



# 1 Validation of the CrIS Fast Physical NH<sub>3</sub> Retrieval with 2 ground-based FTIR

3 Enrico Dammers<sup>1</sup>, Mark W. Shephard<sup>2</sup>, Mathias Palm<sup>3</sup>, Karen Cady-Pereira<sup>4</sup>, Shannon Capps<sup>5\*</sup>, Erik Lutsch<sup>6</sup>,  
4 Kim Strong<sup>6</sup>, James W. Hannigan<sup>7</sup>, Ivan Ortega<sup>7</sup>, Geoffrey C. Toon<sup>8</sup>, Wolfgang Stremme<sup>9</sup>, Michel Grutter<sup>9</sup>,  
5 Nicholas Jones<sup>10</sup>, Dan Smale<sup>11</sup>, Jacob Siemons<sup>2</sup>, Kevin Hrpcek<sup>12</sup>, Denis Tremblay<sup>13</sup>, Martijn Schaap<sup>14</sup>, Justus  
6 Notholt<sup>3</sup>, Jan Willem Erisman<sup>1,15</sup>

7 1. Cluster Earth and Climate, Department of Earth Sciences, Vrije Universiteit Amsterdam, Amsterdam, the  
8 Netherlands  
9 2. Environment and Climate Change Canada, Toronto, Ontario, Canada  
10 3. Institut für Umweltphysik, University of Bremen, Bremen, Germany  
11 4. Atmospheric and Environmental Research (AER), Lexington, Massachusetts, USA  
12 5. Department of Mechanical Engineering, University of Colorado, Boulder, Colorado, USA  
13 6. Department of Physics, University of Toronto, Toronto, Ontario, Canada  
14 7. NCAR, Boulder, Colorado, United States  
15 8. Jet Propulsion Laboratory, California Institute of Technology, Pasadena, California, USA  
16 9. Centro de Ciencias de la Atmósfera, Universidad Nacional Autónoma de México, Mexico City, Mexico  
17 10. University of Wollongong, Wollongong, Australia  
18 11. National Institute of Water and Atmosphere, Lauder, New Zealand  
19 12. University of Wisconsin-Madison Space Science and Engineering Center (SSEC), Madison, Wisconsin, USA.  
20 13. Science Data Processing, Inc., Laurel, MD, United States  
21 14. TNO Built Environment and Geosciences, Department of Air Quality and Climate, Utrecht, the Netherlands  
22 15. Louis Bolk Institute, Driebergen, the Netherlands  
23 \*Now at Civil, Architectural, and Environmental Engineering Department, Drexel University, Philadelphia,  
24 Pennsylvania, USA

25 *Correspondence to: E. Dammers (e.dammers@vu.nl)*

## 26 **Abstract**

27 Global reactive nitrogen emissions into the air have increased to unprecedented levels. Limiting the loss of  
28 reactive nitrogen into the environment is one of the major challenges for humankind. At the current levels  
29 ammonia (NH<sub>3</sub>) is a threat to both the environment and human health. However, relatively little is known about  
30 the total nitrogen budget and distribution around the world, due in part to the sparseness of observations over  
31 most of the globe. Recent advances in the capabilities of measuring NH<sub>3</sub> with satellite instruments have  
32 improved the situation with sensors such as the Infrared Atmospheric Sounding Interferometer (IASI) and the  
33 Cross-Track Infrared Sounder (CrIS) making twice daily observations with global coverage. However, these  
34 require validation to be truly useful, and one of the main challenges in the validation of the satellite NH<sub>3</sub> profile  
35 and total column data products is the scarcity of measurements that can be directly compared. Presented here is  
36 the validation of the CrIS Fast Physical Retrieval (CFPR) NH<sub>3</sub> column and profile measurements using ground-  
37 based Fourier Transform Infrared (FTIR) observations. We use the total columns and profiles from seven FTIR  
38 sites in the Network for the Detection of Atmospheric Composition Change (NDACC) to validate the satellite  
39 data products. The overall FTIR and CrIS total columns compare well with a correlation of  $r = 0.77$  ( $N=218$ )  
40 with very little bias (a slope of 1.02). Binning the comparisons by total column amounts, for concentrations  
41 larger than  $1.0 \times 10^{16}$  molecules cm<sup>-2</sup>, i.e. ranging from moderate to polluted conditions, the relative difference is  
42 on average  $\sim 0 - 5\%$  with a standard deviation of 25-50%, which is comparable to the estimated retrieval



43 uncertainties in both CrIS and the FTIR. For the smallest total column range where there are a large number of  
44 observations at or near the CrIS noise level (detection limit) and the FTIR total columns are smaller than  
45  $1.0 \times 10^{16}$  molecules  $\text{cm}^{-2}$ , the absolute differences between CrIS and the FTIR total columns are small with CrIS  
46 showing a slight positive column bias around  $+2.4 \times 10^{15}$  (standard deviation =  $5.5 \times 10^{15}$ ) molecules  $\text{cm}^{-2}$ ,  
47 which corresponds to a relative difference of  $\sim +50\%$  (std = 100 %). The CrIS retrievals for these comparisons  
48 typically show good vertical sensitivity down to  $\sim 850$  hPa, and at this level the retrieved profiles also compare  
49 well with the median absolute difference of 0.87 ( $\pm 0.08$ ) ppb and a corresponding median relative difference of  
50 39 ( $\pm 2$ )%. Most of the absolute and relative profile comparison differences are in the range of the estimated  
51 retrieval uncertainties. However, the CrIS retrieval does tend to overestimate the concentrations in the levels  
52 near the surface at low concentrations, most probably due to the detection limit of the instrument, and at higher  
53 concentrations shows more of an underestimation of the concentrations in these lower levels.



## 54 1. Introduction

55

56 The disruption of the nitrogen cycle by the human creation of reactive nitrogen has created one of the major  
57 challenges for humankind (Rockström et al., 2009). Global reactive nitrogen emissions into the air have  
58 increased to unsurpassed levels (Fowler et al., 2013) and are currently estimated to be four times larger than pre-  
59 industrial levels (Holland et al., 1999). As a consequence the deposition of atmospheric reactive nitrogen has  
60 increased causing ecosystems and species loss (Rodhe et al 2002; Dentener et al., 2006; Bobbink et al., 2010).  
61 Ammonia (NH<sub>3</sub>) as fertilizer is essential for agricultural production and is one of the most important reactive  
62 nitrogen species in the biosphere. NH<sub>3</sub> emission, atmospheric transport, and atmospheric deposition are major  
63 causes of eutrophication and acidification of soils and water in semi-natural environments (Erisman et al., 2008,  
64 2011). Through reactions with sulphuric acid and nitric acid, ammonium nitrate and ammonium sulphate are  
65 formed which embody up to 50% of the mass of fine mode particulate matter (PM<sub>2.5</sub>) (Seinfeld and Pandis.,  
66 1988; Schaap et al., 2004). PM<sub>2.5</sub> has been associated with various health impacts (Pope et al., 2002; 2009). At  
67 the same time, atmospheric aerosols impact global climate directly through their radiative forcing effect and  
68 indirectly through the formation of clouds (Adams et al., 2001; Myhre et al., 2013). By fertilizing ecosystems,  
69 deposition of NH<sub>3</sub> and other reactive nitrogen compounds also plays a key role in the sequestration of carbon  
70 dioxide (Oren et al., 2001).

71

72 Despite the significance and impact of NH<sub>3</sub> on the environment and climate, its global distribution and budget  
73 are still relatively uncertain (Erisman et al., 2007; Clarisse et al., 2009; Sutton et al., 2013). One of the reasons is  
74 that in-situ measuring of atmospheric NH<sub>3</sub> at ambient levels is complex due to the sticky nature and reactivity of  
75 the molecule, leading to large uncertainties and/or sampling artefacts with the currently used measuring  
76 techniques (von Bobruzki et al., 2010; Puchalski et al., 2011). Measurements are also very sparse. Currently,  
77 observations of NH<sub>3</sub> are mostly available in north-western Europe and central North America, supplemented by  
78 a small number of observations made in China (Van Damme et al., 2015b). Furthermore, there is a lack of  
79 detailed information on its vertical distribution as only a few dedicated airborne measurements are available  
80 (Nowak et al., 2007, 2010; Leen et al., 2013, Whitburn et al., 2015, Shephard et al., 2015). The atmospheric  
81 lifetime of NH<sub>3</sub> is rather short, ranging from hours to a few days. In summary, global emission estimates have  
82 large uncertainties. Estimates of regional emissions attributed to source types different from the main regions  
83 are even more uncertain due to a lack of process knowledge and atmospheric levels (Reis et al., 2009).

84

85 Over the last decade the developments of satellite observations of NH<sub>3</sub> from instruments such as the Cross-track  
86 Infrared Sounder (CrIS, Shephard and Cady-Pereira, 2015), the Infrared Atmospheric Sounding Interferometer  
87 (IASI, Clarisse et al., 2009; Coheur et al., 2009; Van Damme et al., 2014a), the Atmospheric Infrared Sounder  
88 (AIRS, Warner et al., 2016), and the Tropospheric Emission Spectrometer (TES, Beer et al., 2008; Shephard et  
89 al., 2011) show potential to improve our understanding of the NH<sub>3</sub> distribution. Recent studies show the global  
90 distribution of NH<sub>3</sub> measured at a twice daily scale (Van Damme et al., 2014a, Van Damme et al., 2015a) and  
91 reveal seasonal cycles and distributions for regions where measurements were unavailable until now.

92 Comparisons of these observations to surface observations and model simulations, show underestimations of the  
93 modelled NH<sub>3</sub> concentration levels, pointing to underestimated regional and national emissions (Clarisse et al.,



94 2009; Shephard et al., 2011; Heald et al., 2012; Nowak et al., 2012; Zhu et al., 2013; Van Damme et al., 2014b;  
95 Lonsdale et al., 2016; Schiferl et al., 2014, 2016; Zondlo et al., 2016). However, the uncertainty of the satellite  
96 observations is still high due to a lack of validation. The few validation studies showed a limited vertical, spatial  
97 and or temporal coverage of surface observations to do a proper uncertainty analysis (Van Damme et al., 2015b;  
98 Shephard et al., 2015; Sun et al., 2015). A recent study by Dammers et al. (2016a) explored the use of Fourier  
99 transform infrared (FTIR-NH<sub>3</sub>, Dammers et al., 2015) observations to evaluate the uncertainty of the IASI-NH<sub>3</sub>  
100 total column product. The study showed the good performance of the IASI-LUT (Look up table, LUT, Van  
101 Damme et al., 2014a) retrieval with a high correlation ( $r \sim 0.8$ ) but indicated an underestimation of around 30%  
102 due to potential assumptions of the shape of the vertical profile (Whitburn et al., 2016, IASI-NN (Neural  
103 Network, NN)), uncertainty in spectral line parameters and assumptions on the distributions of interfering  
104 species. The study showed the potential of using FTIR observations to validate satellite observations of NH<sub>3</sub> but  
105 also stressed the challenges of validating retrievals that do not provide the vertical measurement sensitivity, such  
106 as the IASI-LUT retrieval. Since no IASI satellite averaging kernels are provided for each retrieval, and thus no  
107 information is available on the vertical sensitivity and/or vertical distribution of each separate observation, it is  
108 hard to determine the cause of the discrepancies between both observations.

109

110 The new CrIS Fast Physical Retrieval (Shephard and Cady-Pereira, 2015) uses an optimal estimation retrieval  
111 approach that provides the information content and the vertical sensitivity (derived from the averaging kernels,  
112 for more details see Shephard and Cady-Pereira, 2015), and robust and straightforward retrieval error estimates  
113 based on retrieval input parameters. The quality of the retrieval has so far not been thoroughly examined against  
114 other observations. Shephard and Cady-Pereira (2015) used Observing System Simulation Experiment (OSSE)  
115 studies to evaluate the initial performance of the CrIS NH<sub>3</sub> retrieval, and report a small positive retrieval bias of  
116 6% with a standard deviation of  $\pm 20\%$  (ranging from  $\pm 12$  to  $\pm 30\%$  over the vertical profile). Note that no  
117 potential systematic errors were included in these OSSE simulations. Their study also shows good qualitative  
118 comparisons with the Tropospheric Emission Spectrometer (TES) satellite (Shephard et al., 2011) and the  
119 ground-level in situ Quantum Cascade-Laser (QCL) observations (Miller et al., 2014) for a case study over the  
120 Central Valley in CA, USA, during the DISCOVER-AQ campaign. However, currently there has not been an  
121 extensive validation of the CrIS NH<sub>3</sub> retrievals using direct comparisons against vertical profile observations. In  
122 this study we will provide both direct comparisons of the CrIS retrieved profiles against ground-based FTIR  
123 observations, and comparisons of CrIS total column values against the FTIR and IASI.

124



125 **2. Methods**

126 **2.1 The CrIS Fast Physical Retrieval**

127 CrIS was launched in late October 2011 on board the Suomi NPP platform. CrIS follows a sun-synchronous  
128 orbit with a daytime overpass time at 13:30 local time (ascending) and a night time equator overpass at 1:30.  
129 The instrument scans along a 2200 km swath using a 3 x 3 array of circular shaped pixels with a diameter of 14  
130 km at nadir for each pixel, becoming larger ovals away from nadir. In this study we use the NH<sub>3</sub> retrieval as  
131 described by Shephard and Cady-Pereira (2015). The retrieval is based on an optimal estimation approach  
132 (Rodgers, 2000) that minimizes the differences between CrIS spectral radiances and simulated forward model  
133 radiances computed from the Optimal Spectral Sampling (OSS) OSS-CrIS (Moncet et al., 2008), which is built  
134 from the well-validated Line-By-Line Radiative Transfer Model (LBLRTM) (Clough et al., 2005; Shephard et  
135 al., 2009; Alvarado et al., 2013). The fast computational speed of OSS facilitates the operational production of  
136 CrIS retrieved (Level 2) products using an optimal estimation retrieval approach (Moncet et al., 2005). The CrIS  
137 OSS radiative transfer forward model computes the spectrum for the full CrIS LW band, at the CrIS spectral  
138 resolution of 0.625 cm<sup>-1</sup> (Tobin, 2012), thus the complete NH<sub>3</sub> spectral band (near 10 μm) is available for the  
139 retrievals. However, only a small number of micro windows are selected for the CrIS retrievals to both  
140 maximize the information content and minimize the influence of errors. Worden et al., (2004) provides an  
141 example of a robust spectral region selection process that takes into consideration both the estimated errors (i.e.  
142 instrument noise, spectroscopy errors, interfering species, etc.) and the associated information content in order  
143 to select the optimal spectral regions for the retrieval. The a-priori profiles selection for the optimal estimation  
144 retrievals follows the Tropospheric Emission Spectrometer (TES) retrieval algorithm (Shephard et al., 2011);  
145 Based on the relative NH<sub>3</sub> signal in the spectra the a-priori is selected from one of three possible profiles  
146 representing unpolluted, moderate, and polluted conditions. The initial guess profiles are also selected from  
147 these three potential profiles.

148

149 An advantage of using an optimal estimation retrieval approach is that averaging kernels (sensitivity to the true  
150 state) and the estimated errors of the retrieved parameter are computed in a robust and straight-forward manner  
151 (for more details see Shephard and Cady-Pereira, 2015). The total satellite retrieved parameter error is  
152 expressed as the sum of the smoothing error (due to unresolved fine structure in the profile), the measurement  
153 error (random instrument noise in the radiance spectrum propagated to the retrieval parameter), and systematic  
154 errors from uncertainties in the non-retrieved forward model parameters and cross-state errors propagated from  
155 retrieval-to-retrieval (i.e. interfering species) (Worden et al., 2004). As of yet we have not included error  
156 estimates for the systematic errors. The CrIS smoothing error is computed, but since in these FTIR comparison  
157 results we apply the FTIR observational operator (which accounts for the smoothing error), the smoothing error  
158 contribution is not included in the CrIS errors reported in the comparisons. Thus, only the measurement errors

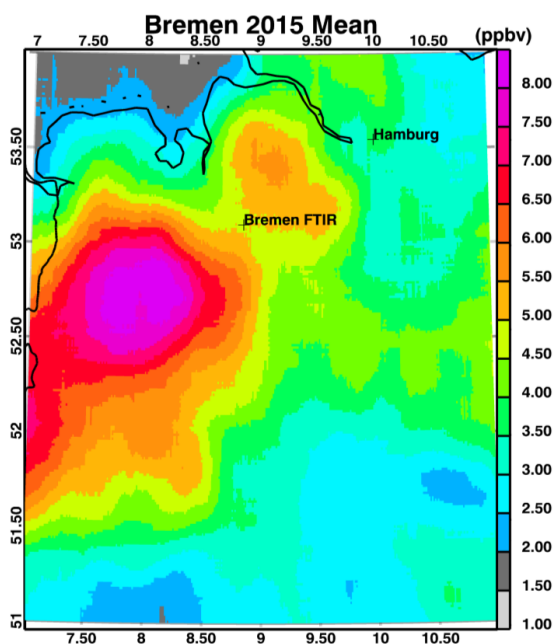


159 are reported for observations used here; these errors can thus be considered the lower limit on the total estimated  
160 CrIS retrieval error.

161 Figure 1 shows an example of CrIS  $\text{NH}_3$  observations surrounding one of the ground-based FTIR instruments.

162 This is a composite map of all days in Bremen with observations in 2015. This figure shows the wide spread

163 elevated amounts of  $\text{NH}_3$  across north-western Germany as observed by CrIS.



164

165 **Figure 1.** Annual mean of the CrIS retrieved  $\text{NH}_3$  surface VMR values around the Bremen FTIR site for 2015.

166 Since the goal of this analysis is to evaluate the CrIS retrievals that provide information beyond the a-priori, we

167 only performed comparisons when the CrIS spectrum presents a  $\text{NH}_3$  signal. We also focused our efforts on

168 FTIR stations that have FTIR observations with total columns larger than  $5 \times 10^{15}$  molecules  $\text{cm}^{-2}$  (~1-2 ppb

169 surface VMR). This restriction does mean that a number of sites of the FTIR- $\text{NH}_3$  dataset will not be used. For

170 comparability of this study to the results of the IASI-LUT evaluation in an earlier study by Dammer et al.,

171 (2016a) we include a short paragraph on the performance of the IASI-LUT and the more recent IASI-NN

172 product when applying similar constraints.

## 173 2.2 FTIR- $\text{NH}_3$ retrieval

174 The FTIR- $\text{NH}_3$  product used in this study is similar to the set described in Dammer et al. (2016a) and is based

175 on the retrieval methodology described by Dammer et al. (2015). The retrieval methodology uses two spectral

176 micro-windows whose spectral width depends on the  $\text{NH}_3$  background concentration determined for the

177 observation stations and location (wider window for stations with background concentrations less than one ppb).

178  $\text{NH}_3$  is retrieved by fitting the spectral lines in the two micro-windows MW1 [930.32-931.32  $\text{cm}^{-1}$  or wide:



179 929.40-931.40  $\text{cm}^{-1}$ ] and MW2 [962.70-970.00  $\text{cm}^{-1}$  or wide: 962.10-970.00  $\text{cm}^{-1}$ . An optimal estimation  
180 approach (Rodgers et al., 2000) is used, implemented in the SFIT4 algorithm (Pougatchev et al., 1995; Hase et  
181 al., 2004, 2006). There are a number of species that can interfere to some extent in both windows, with the  
182 major species being  $\text{H}_2\text{O}$ ,  $\text{CO}_2$  and  $\text{O}_3$  and the minor species  $\text{N}_2\text{O}$ ,  $\text{HNO}_3$ , CFC-12, and  $\text{SF}_6$ . The HITRAN 2012  
183 database (Rothman et al., 2014) is used for the spectral lines. A further set of spectroscopic line parameter  
184 adjustments are added for  $\text{CO}_2$  taken from the ATMOS database (Brown et al., 1996) as well as a set of pseudo-  
185 lines for the broad absorptions by the CFC-12 and  $\text{SF}_6$  molecules (created by NASA-JPL, G.C. Toon,  
186 <http://mark4sun.jpl.nasa.gov/pseudo.html>). The  $\text{NH}_3$  a-priori profiles are based on balloon measurements (Toon  
187 et al., 1999) and refitted to match the local surface concentrations (depending on the station either measured or  
188 estimated by model results). For the interfering species a-priori profiles we use the Whole Atmosphere  
189 Community Climate Model (WACCM, Chang et al., 2008, v3548). The estimated errors in the FTIR- $\text{NH}_3$   
190 retrievals are in the order of ~30% (Dammers et al., 2015) with the uncertainties in the  $\text{NH}_3$  line spectroscopy  
191 being the most important contributor. Based on the data requirements in section 2.1, a set of seven stations is  
192 used (Table 1). For all sites except Wollongong in Australia we use the basic narrow spectral windows. For  
193 Wollongong the wide spectral windows are used. For a more detailed description of each of the stations see the  
194 publications listed in Table 1 or Dammers et al. (2016a).

195 **Table 1.** The location, longitudinal and latitudinal position, altitude above sea level, and type of instrument for  
196 each of the FTIR sites used in this study. In addition, a reference is given to a detailed site description, when  
197 available.

Station	Lon (degrees)	Lat (degrees)	Altitude (m.a.s.l.)	FTIR instrument	Reference
Bremen, Germany	8.85E	53.10N	27	Bruker 125 HR	Velazco et al., 2007
Toronto, Canada	79.60W	43.66N	174	ABB Bomem DA8	Wiacek et al., 2007 Lutsch et al., 2016
Boulder, United States	105.26W	39.99N	1634	Bruker 120 HR	
Pasadena, United States	118.17W	34.20N	350	MkIV_JPL	
Mexico City, Mexico	99.18W	19.33N	2260	Bruker Vertex 80	Bezanilla et al., 2014
Wollongong, Australia	150.88E	34.41S	30	Bruker 125 HR	
Lauder, New Zealand	169.68E	45.04S	370	Bruker 120 HR	Morgenstern et al., 2012

198

### 199 2.3 IASI- $\text{NH}_3$

200 The CrIS retrieval will also be compared with corresponding IASI/FTIR retrievals using results from a previous  
201 study by Dammers et al. (2016a). Both the IASI-LUT (Van Damme et al., 2014a) and the IASI-NN (Neural  
202 Networks, Whitburn et al., 2016) retrievals from observations by the IASI instrument aboard MetOp-A will be  
203 used. A short description of both IASI retrievals is provided here, for a more in-depth description, see the  
204 respective publications by Van Damme et al. (2014a) and Whitburn et al. (2016). The IASI instrument on board  
205 the MetOp-A platform is in a sun-synchronous orbit and has a daytime overpass at around 9:30 local solar time  
206 and a night time overpass at around 21:30. The instrument has a circular footprint of about 12 km diameter for  
207 nadir viewing angles with of nadir observations along a swath of 2100 km. Both IASI retrievals are based on the  
208 calculation of a dimensionless spectral index called the Hyperspectral Range Index (HRI) (Van Damme et al.,  
209 2014a). The HRI is representative of the amount of  $\text{NH}_3$  in the measured column. The IASI-LUT retrieval  
210 makes a direct conversion of the HRI to a total column density with the use of a look-up-table (LUT). The LUT  
211 is created using a large number of simulations for a wide range of atmospheric conditions which links the



212 Thermal Contrast (TC, the difference between the air temperature at 1.5 km altitude and the temperature of the  
213 Earth surface) and the HRI to a  $\text{NH}_3$  total column density. The retrieval includes a retrieval error based on the  
214 uncertainties in the initial HRI and TC parameters. The more recent IASI-NN retrieval (Whitburn et al., 2016)  
215 follows similar steps but it makes use of a neural network. The neural network combines the complete  
216 temperature, humidity and pressure profiles for a better representation of the state of the atmosphere. At the  
217 same time the retrieval error estimate is improved by including error terms for the uncertainty in the profile  
218 shape, and the full temperature and water vapour profiles. The IASI-NN version uses the fixed profiles that were  
219 described by Van Damme et al., (2014) but allows for the use of third party profiles to improve the  
220 representation of the  $\text{NH}_3$  atmospheric profile. The IASI-LUT and IASI-NN retrievals have both been  
221 previously compared with FTIR observations (Dammers et al., 2016a, Dammers et al., 2016b). They compared  
222 reasonably well with correlations around  $r=0.8$  for a set of FTIR stations, with an underestimation of around  
223 30% that depends slightly on the magnitude of total column amounts, with the IASI-NN performing slightly  
224 better.

225

#### 226 **2.4 Data criteria & quality**

227  $\text{NH}_3$  concentrations show large variations both in space and time as the result of the large heterogeneity in  
228 emission strengths due to spatially variable sources and drivers such as meteorology and land use (Sutton et al.,  
229 2013). This high variability poses challenges in matching ground-based point observations made by FTIR  
230 observations with CrIS downward-looking satellite measurements which have a 14-km nadir footprint. For the  
231 pairing of the measurement data we apply data selection criteria similar to that described in Dammers et al.  
232 (2016a) and summarized in Table 2. To minimize the impact of the heterogeneity of the sources, we choose a  
233 maximum of 50 km between the centre points of the CrIS observations and the FTIR site location. To diminish  
234 the effect of temporal differences between the FTIR and CrIS observations a maximum time difference of 90  
235 minutes is used. Topographical effects are reduced by choosing a maximum altitude difference of 300 m at any  
236 point between the FTIR site location and the centre point of the satellite pixel location. The altitude differences  
237 are calculated using the Space Shuttle Radar Topography Mission Global product at 3 arc-second resolution  
238 (SRTMGL3, Farr et al., 2007). To ensure the data quality of CrIS- $\text{NH}_3$  retrieval for Version 1.0, a small number  
239 of outliers with a maximum retrieved concentration above 200 ppb (at any point in the profile) were removed  
240 from the comparison dataset. While potentially a surface  $\text{NH}_3$  value of 200 ppb (and above) would be possible  
241 (i.e. downwind of forest fires), it is highly unlikely to occur over the entire footprint of the satellite instrument.  
242 Moreover, after inspecting these data points, they seem to be affected by numerical issues in the fitting  
243 procedure (possibly due to interfering species). As we are interested in validating the CrIS observational  
244 information (not just a-priori information), we only select comparisons that contain some information from the  
245 satellite (degrees of freedom for signal (DOFS)  $\geq 0.1$ ). Do note that on average the observations have a DOFS  
246 between 0.9 and 1.1. The DOFS  $> 0.1$  filter only removes some of the outliers at the lower end. No explicit filter  
247 is applied to account for clouds; however, clouds will implicitly be accounted for by the quality control as CrIS  
248 will not measure a  $\text{NH}_3$  signal (e.g. DOFS  $< 0.1$ ) below optically thick clouds (e.g. cloud optical depth  $> \sim 1$ ). In  
249 addition, the CrIS observations are matched with FTIR observations taken only during clear-sky conditions,  
250 which mostly eliminates influence from cloud cover. Finally, the high signal to noise ratios (SNR) of the CrIS  
251 instrument, allows it to retrieve  $\text{NH}_3$  from a thermal contrast approaching 0 K during daytime observations





252 (Clarisse et al., 2010). Given this, we decided not to apply a thermal contrast filter to the CrIS data. No  
 253 additional filters are applied to the FTIR observations beyond the clear-sky requirement.

254

255 For both IASI retrievals, we use the same observation selection criteria as described in Dammers et al. (2016a).

256 The set of criteria is similar to those used here for the CrIS observations. Observations from both IASI retrievals  
 257 are matched using the overpass time, and longitudinal and latitudinal positions. For comparability with CrIS a  
 258 spatial difference limit of 50 km limit was used, instead of the 25 km spatial limit used in the previous study.

259 Furthermore we apply the thermal contrast (> 12K, difference between the temperatures at 1.5 km and the  
 260 surface) and Earth skin temperature criteria to the IASI observations to match the previous study.

261

262 **Table 2. Coincidence criteria and quality flags applied to the satellite and FTIR data. The third through**  
 263 **fifth columns show the number of observations remaining after each subsequent data criteria step and**  
 264 **the number of possible combinations between the CrIS and FTIR observations. The first set of numbers**  
 265 **indicate the number of CrIS observations within a 1°x 1° degree square surrounding the FTIR site.**

Filter	Data Criteria	Nr. Obs.		
		FTIR	CrIS	Combinations
CrIS		15661	25855	
Temporal sampling difference	Max 90 min	1576	13959	112179
Spatial sampling difference	Max 50 km	1514	3134	22869
Elevation difference	Max 300 m	1505	1642	9713
Quality flag	DOFS ≥ 0.1	1433	1453	8579

266

## 267 2.5 Observational Operator Application

268

269 To account for the vertical sensitivity and the influence of the a-priori profiles of both retrievals we apply the  
 270 observational operator (averaging kernel and a-priori of the retrieval) of the FTIR retrieval to the CrIS retrieved  
 271 profiles. The CrIS observations are matched to each individual FTIR observation in time and space following  
 272 the matching criteria. The FTIR averaging kernels, a-priori profiles, and retrieved profiles are first mapped to  
 273 the CrIS pressure levels (fixed pressure grid, layers are made smaller or cut off for observations above elevation  
 274 to fit the fixed pressure grid). Following Rodgers and Connor (2003) and Calisesi et al. (2005) this results in the  
 275 mapped FTIR averaging kernel,  $A_{ftir}^{mapped}$ , the mapped FTIR apriori,  $x_{ftir}^{mapped,apriori}$ , and the mapped FTIR  
 276 retrieved profile,  $x_{ftir}^{mapped}$ . Then we apply the FTIR observational operator to the CrIS observations using eq.  
 277 (1).

$$278 \hat{x}_{CrIS} = x_{ftir}^{mapped,apriori} + A_{ftir}^{mapped} (x_{CrIS} - x_{ftir}^{mapped,apriori}) \quad (1)$$

$$279 \hat{\Delta x}_{abs} = \hat{x}_{CrIS} - x_{ftir}^{mapped} \quad (2)$$

$$280 \hat{\Delta x}_{rel} = (\hat{x}_{CrIS} - x_{ftir}^{mapped}) / (0.5 x_{ftir}^{mapped} + 0.5 \hat{x}_{CrIS}) \quad (3)$$

281 where  $x_{ftir}^{apriori}$  is the FTIR a-priori profile,  $x_{ftir}^{mapped}$  is the interpolated FTIR profile,  $A_{ftir}^{mapped}$  is the FTIR  
 282 averaging kernel, and  $\hat{x}_{CrIS}$  is the smoothed CrIS profile.

283

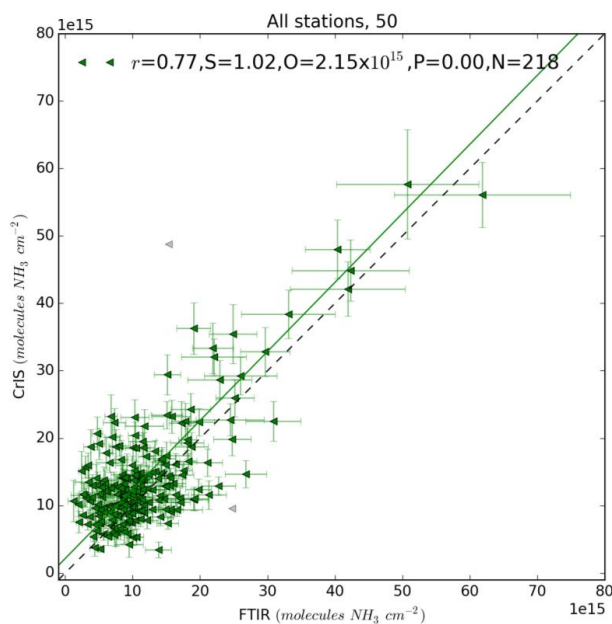


284 The CrIS smoothed profile  $\hat{x}_{CrIS}$  calculated from equation (1) provides an estimate of the FTIR retrieval applied  
285 to the CrIS satellite profile. Next we evaluate both total column and profile measurements.

286 For the first validation step, following Dammers et al. (2016a), who evaluated the IASI-LUT (Van Damme et  
287 al., 2014a) product, we sum the individual profile ( $\hat{x}_{CrIS}$ ) to obtain a column total to compare to the FTIR total  
288 columns. This step gives the opportunity to evaluate the CrIS retrieval in a similar manner as was done with the  
289 IASI-LUT retrieval. If multiple FTIR observations match a single CrIS overpass we also average those together  
290 into a single value as well as each matching averaged CrIS observation. Therefore, it is possible to have multiple  
291 FTIR observations, each with multiple CrIS observations all averaged into a single matching representative  
292 observation. For the profile comparison this averaging is not performed to keep as much detail available as  
293 possible. An important point to make is that this approach assumes that the FTIR retrieval gives a better  
294 representation of the truth. While this may be true, the FTIR retrieval will not match the truth completely. For  
295 readability we assume that the FTIR retrieval indeed gives a better representation of the truth, and in the next  
296 sections will describe the case in which we apply the FTIR observational operator to the CrIS values. For the  
297 tenacious reader we included a similar set of results in the appendix, using the CrIS observational operator  
298 instead of the FTIR observational operator, as the assumption of the FTIR being truth is not exactly right.  
299

### 300 3. Results and discussion

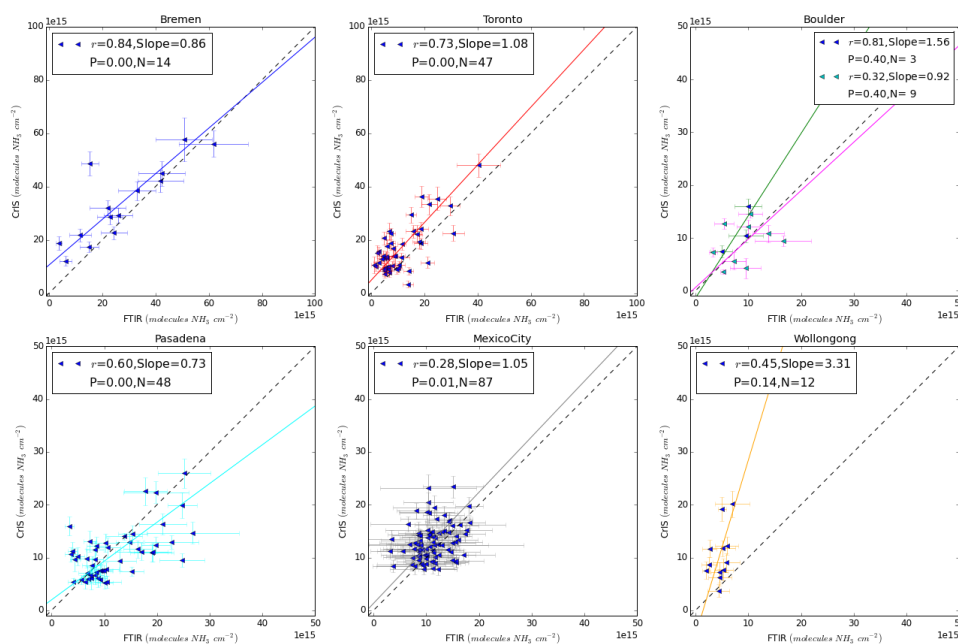
#### 301 3.1 Total column comparison



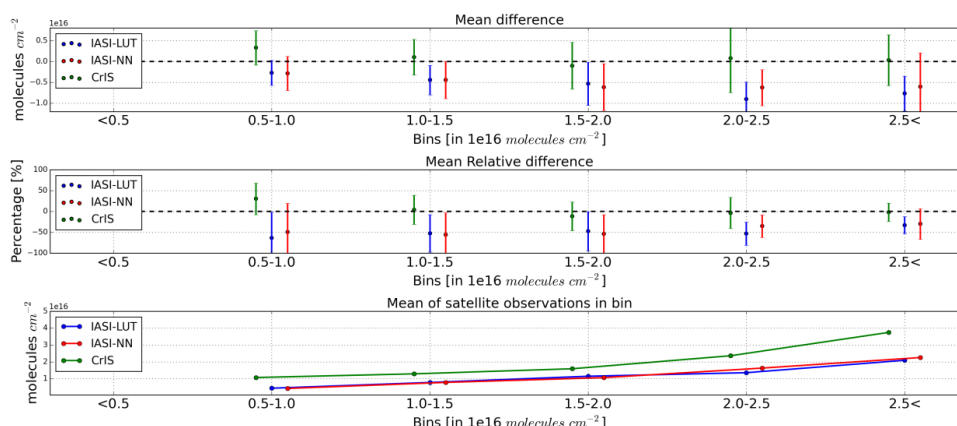
302  
303 **Figure 2.** Correlation between the FTIR and CrIS total columns using the coincident data from all measurement  
304 sites. The horizontal and vertical bars show the error on each FTIR and CrIS observation. The trend line shows  
305 the results of the regression analysis.  
306



307 The total columns are averaged as explained in Section 2.4 to show a direct comparison of FTIR measurements  
 308 with CrIS observations in Figure 2. A three sigma outlier filter was applied to calculate the regression statistics.  
 309 The filtered outliers are displayed in grey, and may be caused by low information content (DOFS) and terrain  
 310 characteristics. For the regression we used the reduced major axis regression (Bevington and Robinson, 1992),  
 311 accounting for possible errors both in the x and y values. The overall agreement is good with a correlation of  $r =$   
 312  $0.77$  ( $P < 0.01$ ,  $N = 218$ ) and a slope of  $1.02 (+/- 0.05)$ . At the lower range of values the CrIS column totals are  
 313 significantly higher than the observed FTIR values. Possibly the CrIS retrieval overestimates due to the low  
 314 sensitivity to low concentrations. Without the sensitivity the retrieval will find a value more closely to the a-  
 315 priori, which may be too high. Figure 3 shows the comparisons at each station. When the comparisons are  
 316 broken down by station (Figure 3), the correlation varies from site to site, from a minimum of  $0.28$  in Mexico  
 317 City (possibly due to retrieval errors associated with the highly irregular terrain) to a maximum of  $0.84$  in  
 318 Bremen. In Toronto, Bremen and Pasadena there is good agreement when  $\text{NH}_3$  is elevated ( $> 20 \times 10^{15}$   
 319 molecules  $\text{cm}^{-2}$ ) in, and low bias in the CrIS total columns for intermediate values (between  $10$  and  $20 \times 10^{15}$   
 320 molecules  $\text{cm}^{-2}$ ).



321  
 322 **Figure 3.** FTIR vs CrIS comparison scatter plots showing the correlations for each of the individual stations,  
 323 with estimates error plotted for each value. The trend lines show the individual regression results. Note the  
 324 different ranges on the x and y axis. The results for the Boulder (green line) and Lauder (pink line) sites are  
 325 shown in the same panel.  
 326



327

328 **Figure 4.** Plots of the mean absolute and relative differences between CrIS and IASI, as a function of NH<sub>3</sub> total  
 329 column. Observations are separated into bins of total columns. The upper panel shows the mean absolute  
 330 difference (MD). The middle panel shows the mean relative difference. The bars in these top two panels show  
 331 the standard deviation for each value. The bottom panel shows the mean of the observations in each bin.

332

333 The mean absolute (MD) and relative difference (MRD) are calculated following equation 4 and equation 5;

$$334 \quad MRD = \frac{1}{N} \sum_{i=1}^N \frac{(CrIS \text{ column}_i - FTIR \text{ column}_i) \times 100}{0.5 * FTIR \text{ column}_i + 0.5 * CrIS \text{ column}_i} \quad (4)$$

$$335 \quad MD = \frac{1}{N} \sum_{i=1}^N (CrIS \text{ column}_i - FTIR \text{ column}_i) \quad (5)$$

336 with N being the number of observations.

337

338 **Table 3.** Results of the total column comparisons of the FTIR to CrIS, FTIR to IASI-LUT and FTIR to IASI-  
 339 NN. N is the number of averaged total columns, MD is the mean difference [ $10^{15}$  molecules  $\text{cm}^{-2}$ ], MRD is the  
 340 mean relative difference [frac, in %]. Take note that the combined value N does not add up with all the separate  
 341 sites as observations have been included for FTIR total columns  $> 5 \times 10^{15}$  molecules  $\text{cm}^{-2}$ .

Retrieval	Column total range in molecules $\text{cm}^{-2}$	N	MD in $10^{15}$ ( $1\sigma$ )	MRD in % ( $1\sigma$ )	FTIR mean in $10^{15}$ ( $1\sigma$ )
CrIS-NH <sub>3</sub>	$< 10.0 \times 10^{15}$	93	3.3 (4.1)	30.2 (38.0)	7.5 (1.5)
CrIS-NH <sub>3</sub>	$\geq 10.0 \times 10^{15}$	109	0.4 (5.3)	-1.39 (34.4)	16.7 (8.5)
IASI-LUT	$< 10.0 \times 10^{15}$	229	-2.7 (3.0)	-63.6 (62.6)	7.1 (1.4)
IASI-LUT	$\geq 10.0 \times 10^{15}$	156	-5.1 (4.2)	-50.2 (43.6)	14.8 (6.7)
IASI-NN	$< 10.0 \times 10^{15}$	212	-2.2 (3.6)	-57.0 (68.7)	7.1 (1.4)
IASI-NN	$\geq 10.0 \times 10^{15}$	156	-5.0 (5.1)	-52.5 (49.7)	14.8 (6.7)

342

343 We evaluate the data by subdividing the comparisons over a set of total column bins as a function of the FTIR  
 344 total column value of each individual observation. The bins (with a range of  $5 \times 10^{15}$  to  $25 \times 10^{15}$  molecules  $\text{cm}^{-2}$   
 345 with iterations steps of  $5 \times 10^{15}$  molecules  $\text{cm}^{-2}$ ) give a better representation of the performance of the retrieval  
 346 as it shows the influence of the retrieval as a function of magnitude of the total column densities. The results of  
 347 these total column comparisons are presented in Figure 4. Table 3 summarizes the results for each of the FTIR  
 348 to satellite column comparisons into two total column bins, which splits the comparisons between smaller and  
 349 larger than  $10 \times 10^{15}$  molecules  $\text{cm}^{-2}$ . A few combinations of the IASI-NN and FTIR retrievals have a small



350 denominator value that causes problems in the calculation of the MRD. A three sigma outlier filter based on the  
351 relative difference is applied to remove these outliers ( $<10 \times 10^{15}$  molecules  $\text{cm}^{-2}$ , only the IASI-NN set). The  
352 statistical values are not given separately by site because of the low number of matching observations for a  
353 number of the sites.

354

355 The CrIS/FTIR comparison results show a large positive difference in both the absolute (MD) and relative  
356 (MRD) for the smallest bin, ( $5.0\text{-}10.0 \times 10^{15}$  molecules  $\text{cm}^{-2}$ ). The rest of the CrIS/FTIR comparison bins with  
357  $\text{NH}_3$  values  $> 10.0 \times 10^{15}$  agree very well with a nearly constant bias (MD) around zero, and a standard  
358 deviation of the order of  $5.0 \times 10^{15}$  that slightly dips below zero in the middle bin. The standard deviation over  
359 these bins is also more or less constant, and the weak dependence on the number of observations in each bin  
360 indicates that most of the effect is coming from the random error on the observations. The relative difference  
361 becomes systematically smaller with increasing column total amounts, and tend towards zero with a standard  
362 deviation  $\sim 25\text{-}50\%$ , which is on the order of the reported estimated errors of the FTIR retrieval (Dammers et al.,  
363 2015).

364

365 For a comparison against previous reported satellite results, we included both the IASI-LUT (Van Damme et al.,  
366 2014a) and the IASI-NN (Whitburn et al., 2016) comparisons against the FTIR observations. Both IASI  
367 products show similar differences as a function of  $\text{NH}_3$  column bins, which is somewhat different from the  
368 CrIS/FTIR comparison results. The absolute difference (MD) is mostly negative with the smallest factor for the  
369 smallest total column bin, with a difference around  $-2.5 \times 10^{15}$  ( $\pm 3.0 \times 10^{15}$ ) molecules  $\text{cm}^{-2}$  that slowly increases  
370 as a function of the total column. However, the relative difference (MRD) is at its maximum for the smaller bin  
371 with a difference of the order  $-50\%$  ( $\pm 50\%$ ) which decreases to  $\sim -10\text{-}25\%$  ( $\pm 25\%$ ) with increasing bin value.  
372 For both the IASI-NN and IASI-LUT retrievals we find an underestimation of the total columns, which  
373 originates mostly from a large systematic error in combination with more randomly distributed error sources  
374 such as the instrument noise and interfering species, which is similar to results reported earlier for IASI-LUT  
375 (Dammers et al., 2016b).

376

377 A number of factors, besides the earlier reported FTIR uncertainties, can explain the differences between the  
378 FTIR and CrIS measurements. The small positive bias found for CrIS points to a small systematic error. The  
379 higher SNR, from both the low radiometric noise and high spectral resolution, along with the shorter  
380 atmospheric path lengths for observations from the ground-based solar-pointing FTIR instrument, enables it to  
381 resolve smaller gradients in the retrieved spectra, which potentially can provide greater vertical information and  
382 detect smaller column amounts (lower detection limit). This could explain the larger MRD and MD CrIS  
383 differences at the lower end of the total column range. However, a number of standalone tests with the FTIR  
384 retrieval showed only a minor increase in the total column following a decrease in spectral resolution, which  
385 indicates that the spectral resolution itself is not enough to explain the difference.

386

### 387 **3.2 Profile Comparison**

388 The CrIS satellite and FTIR retrieved profiles are matched using the criteria specified above in Table 2 and  
389 compared. It is possible for a CrIS observation to be included multiple times in the comparison as there can be



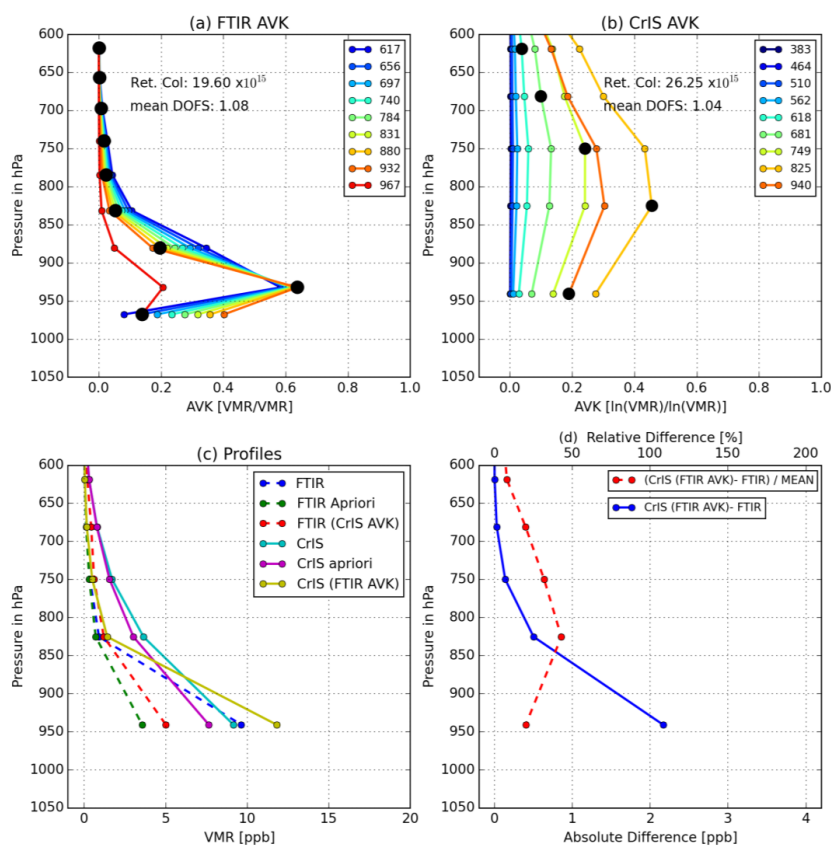
390 more than one FTIR observation per day, and /or, the possibility of multiple satellite overpasses that match a  
391 single FTIR observation.

#### 392 **A representative profile example**

393 An example of the profile information contained in a representative CrIS and FTIR profile is shown in Fig. 5.  
394 Although the vertical sensitivity and distribution of  $\text{NH}_3$  differs per station this is a fairly representative. The  
395 FTIR usually has a somewhat larger DOFS in the order of 1.0-2.0, mostly depending on the concentration of  
396  $\text{NH}_3$ , compared to the CrIS total of  $\sim 1$  DOFS. Figure 5a shows an unsmoothed FTIR averaging kernel [vmr vmr<sup>-1</sup>]  
397 <sup>1</sup>] of a typical FTIR observation. The averaging kernel (AVK) peaks between the surface and  $\sim 850$  hPa, which is  
398 typical for most observations. In specific cases with plumes overpassing the site, the averaging kernel peak is at  
399 a higher altitude matching the location of the  $\text{NH}_3$  plume. The CrIS averaging kernel (Fig. 5b) usually has a  
400 maximum somewhere in between 680-850 hPa depending on the local conditions. This particular observation  
401 has a maximum near the surface, an indication of a day with good thermal contrast. Both the FTIR and CrIS  
402 concentration profiles have a maximum at the surface with a continuous decrease that mostly matches the a-  
403 priori profile in shape following the low DOFS. This is visible for layers at the lower pressures (higher altitudes)  
404 where the FTIR and CrIS a-priori and retrieved volume mixing ratios become similar and near zero. The  
405 absolute difference between the FTIR and CrIS profiles can be calculated by applying the FTIR observational  
406 operator to the CrIS profile, as we described in section 2.5. The largest absolute difference (Fig. 5d) is found at  
407 the surface, which is also generally where the largest absolute  $\text{NH}_3$  values occur. The FTIR smoothed relative  
408 difference (red, striped line) peaks at the pressure where the sensitivity of the CrIS retrieval is highest ( $\sim 55\%$ ),  
409 which goes down to  $\sim 20\text{-}30\%$  for the higher altitude and surface pressure layers. Overall the retrievals agree  
410 well with most of the difference explained by the errors of the individual retrievals. For an illustration of the  
411 systematic and random errors on the FTIR and CrIS profiles shown in Fig 5, see the figures in the appendix: for  
412 the FTIR error profile see Fig. A1 (absolute error) and A2 (relative error) and for the CrIS measurement error  
413 profile see Fig. A3. Please note that we only show the diagonal error covariance values for each of the errors,  
414 which is common practice. The total column of our example profile is  $\sim 20 \times 10^{15}$  molecules  $\text{cm}^{-2}$  which is a  
415 slightly larger value than average. The total random error is  $< 10\%$  for each of the layers, mostly dominated by  
416 the measurement error, which is somewhat smaller than average (Dammers et al., 2015) following the larger  
417  $\text{NH}_3$  VMR. A similar value is found for the CrIS measurement error with most layers showing an error  $< 10\%$ .  
418 The FTIR systematic error is around  $\sim 10\%$  near the surface and grows to a larger 40% for the layers between  
419 900 – 750 hPa. The error is mostly due to the errors in the  $\text{NH}_3$  spectroscopy (Dammers et al., 2015). The shape  
420 of the relative difference between the FTIR and CrIS closely follows the shape systematic error on the FTIR  
421 profile pointing to that error as the main cause of difference.



FTIR:CrIS retrieved profiles: 20130709: Pasadena



422

423 **Figure 5.** Example of the  $\text{NH}_3$  profile comparison for an FTIR profile matched with a CrIS profile measured  
 424 around the Pasadena site. With (a) the FTIR averaging kernel, (b) the CrIS averaging kernel. For both averaging  
 425 kernels the black dots show the matrices diagonal values. Panel (c) shows the retrieved profiles of both FTIR  
 426 (blue) and CrIS (cyan) with the FTIR values mapped to the CrIS pressure layers. Also shown are the FTIR a-  
 427 priori (green), the CrIS a-priori (purple), the CrIS retrieved profile smoothed with the FTIR averaging kernel  
 428 [CrIS (FTIR AVK)] (yellow) and the FTIR profile smoothed with the CrIS averaging kernel [FTIR (CrIS  
 429 AVK)](red). In panel (d), the blue line is the absolute difference between the FTIR profile (blue, panel (c)) and  
 430 the CrIS profile smoothed with the FTIR averaging kernel (Yellow, panel (c)) with the red line the  
 431 corresponding relative difference.

432 **All paired data**

433 In Fig. 6 all the individual site comparisons were merged. The Mexico City site was left out of this figure  
 434 because of the large number of observations in combination with a difference in pressure grid due to the high  
 435 altitude of the city which obscured the overall analysis and biased the results towards the results of one station.  
 436 Similar to the single profile example the FTIR profile peaks near the surface for most observations, slowly  
 437 going towards zero with decreasing pressure. Compared to the representative profile example a number of



438 differences emerge. A number of FTIR observations peak further above the surface and are shown as outliers  
439 which drag the mean further away from the median values. The combined CrIS profile in Fig. 6 shows a similar  
440 behaviour, although for the lowest pressure layer it has a lower median and mean compared to the layer above.  
441 The difference between Fig. 5 and Fig. 6e derives mostly from the number of observations used in the boxplot,  
442 many with weak sensitivity at the surface. Similar to the single profile example in Fig. 5, the FTIR averaging  
443 kernels in Fig. 6c on average peak near or just above the surface (with the diagonal elements of the AVK's  
444 shown in the figure). The sensitivity varies a great deal between the observations as shown by the large spread  
445 of the individual layers. The CrIS averaging kernels (Fig. 6g) usually peak in the boundary layer around the 779  
446 hPa layer with the 2 surrounding layers having somewhat similar values. The instrument is less sensitive to the  
447 surface layer as is demonstrated by the large decrease in the AVK near the surface, but this varies depending on  
448 the local conditions. We find the largest absolute differences in the lower three layers, as was seen in the  
449 example in Fig. 5, although the differences decrease downwards rather than increase. The relative difference  
450 shows a similar shape to Fig 5. Overall both retrievals agree quite well. The relative differences in the single  
451 level retrieved profile values in Fig. 6h show an average difference in the range of ~20 to 40% with the 25<sup>th</sup> and  
452 75<sup>th</sup> percentiles at around 60-80%, which partially follows from our large range of concentrations. The absolute  
453 difference shows an average difference in the range of -0.66 to 0.87 ppb around the peak sensitivity levels of the  
454 CrIS observations (681 to 849 hPa). The lower number of surface observations follow from the fact that only the  
455 Bremen site is located at an altitude low enough for the CrIS retrieval to provide a result at this pressure level..  
456 Because of this difference in retrieval layering, the remaining 227 observations mostly follow from matching  
457 observations in Bremen, which is located in a region of significant NH<sub>3</sub> emissions.

458



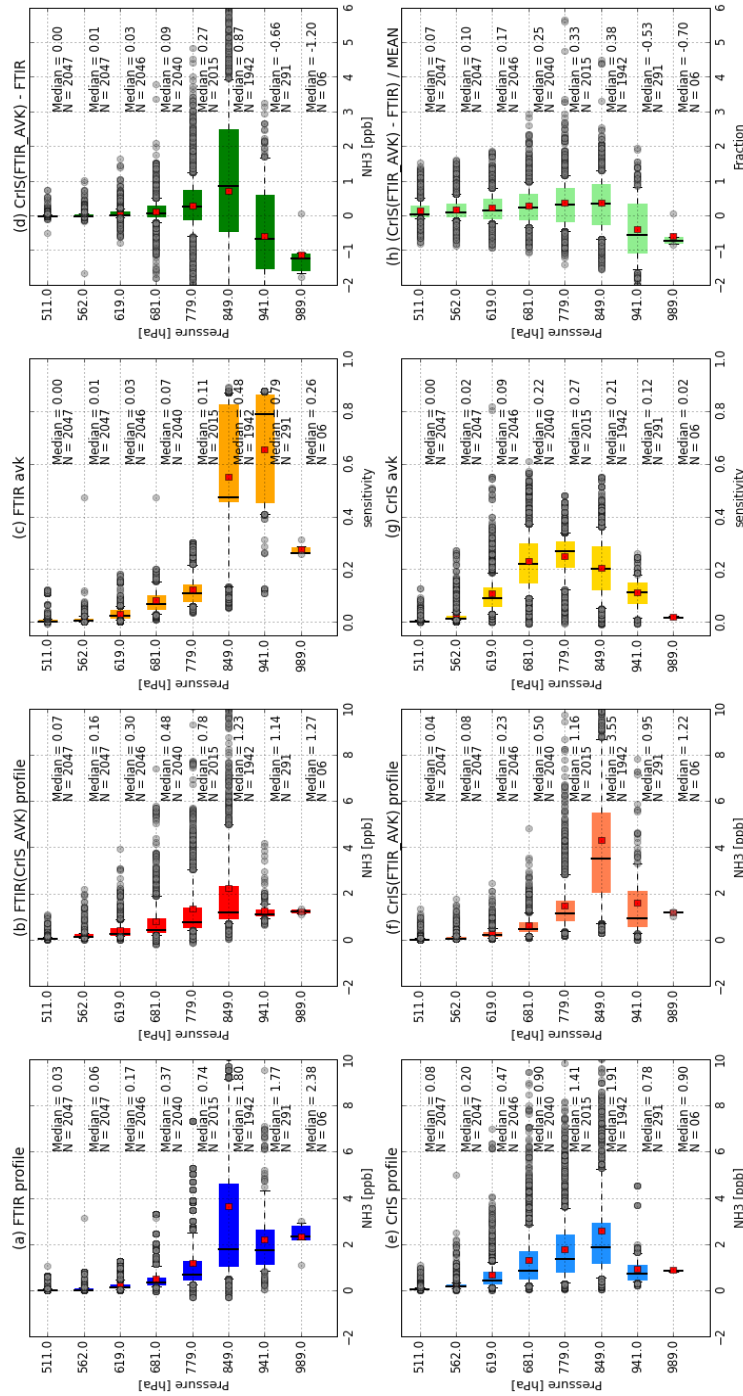
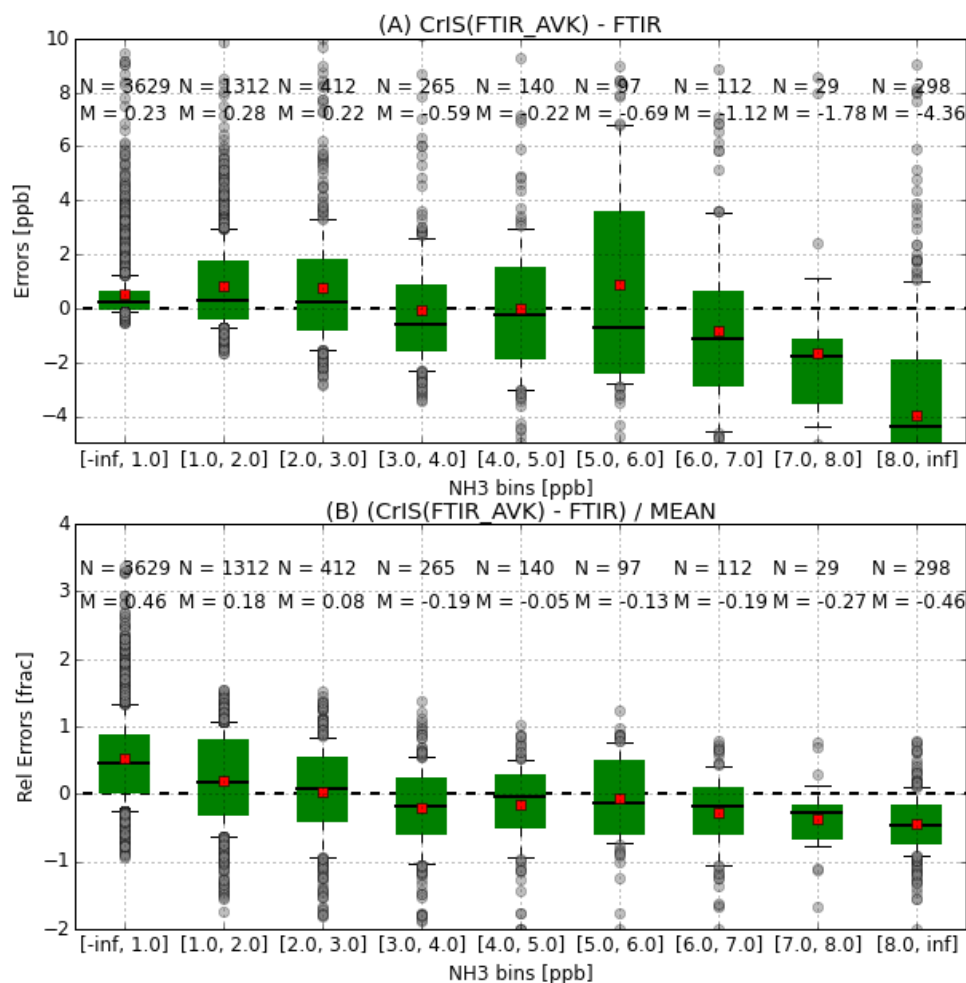


**Figure 6.** Profile comparison for all stations combined. Observations are combined following pressure “bins”, i.e. the midpoints of the CrIS pressure grid. Subplot (a) shows the mean profiles of FTIR (blue), (b) the profiles of FTIR with the CrIS averaging kernel applied to it (red), (c) the FTIR averaging kernel diagonal values, and (d) shows the absolute difference [VMR] between profiles (f) and (a). The second row shows the CrIS mean profile in (e), (f) the profiles of CrIS with the FTIR averaging kernel applied, (g) the CrIS averaging kernel diagonal values, (h) the relative difference [Fraction] between the profiles in (f) and (a). Each of the boxes edges are the 25th and 75th percentiles, the black lines in each box is the median, the red diamond is the mean, the whiskers are the 10th and 90th percentiles, and the grey circles are the outlier values outside the whiskers.

459  
 460  
 461  
 462  
 463  
 464  
 465



466

467 **Figure 7.** Summary of the errors as a function of the VMR of NH<sub>3</sub> in the individual FTIR layers. The box edges  
 468 are the 25<sup>th</sup> and 75<sup>th</sup> percentiles, the black line in the box is the median, the red diamond is the mean, the  
 469 whiskers are the 10<sup>th</sup> and 90<sup>th</sup> percentiles, and the grey circles are the outlier values outside the whiskers. Only  
 470 observations with a pressure greater than 650 hPa are used. The top panel shows the absolute difference for each  
 471 VMR bin, the bottom panel shows the relative difference for each VMR bin.

472

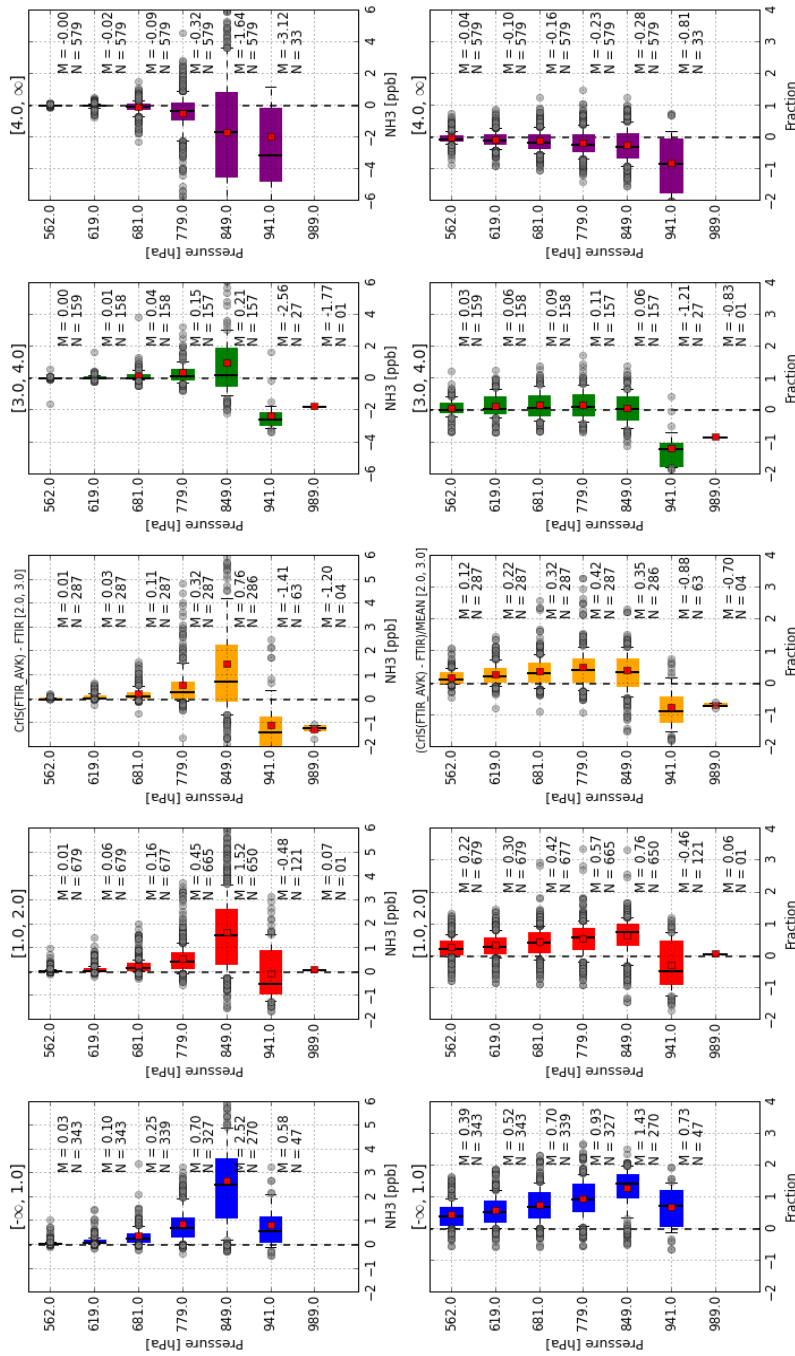
473 The switch between negative and positive values in the absolute difference (see Fig. 6d), occurs in the two  
 474 lowest layers dominated by the Bremen observations and provides insight into the relation between absolute  
 475 differences as function of retrieved concentration. Fig. 7 shows a summary of the differences as a function of the  
 476 individual NH<sub>3</sub> VMR layer amounts. As seen before in the column comparison, e.g. Fig 2 and 4, the CrIS  
 477 retrieval gives larger total columns than the FTIR retrieval for the small values of VMR. For increasing VMRs,  
 478 this slowly tends to a negative absolute difference with a relative difference in the range of 20-30%. However,  
 479 note that the number of compared values in these high VMR bins are by far lower than in the first three bins



480 leading to relatively less effect in the total column and merged VMR figures (Figs. 2 and 6) from these high  
481 VMR bins. We now combine the results of Figs. 6 and 7 into Figure 8 to create a set of subplots showing the  
482 difference between both retrieved profiles as a function of the maximum VMR of each retrieved FTIR profile.  
483 For the layers with pressure less than 681 hPa we generally find good agreement, which is expected but not very  
484 meaningful, since there is not much  $\text{NH}_3$  (and thus sensitivity) in these layers and any differences are smoothed  
485 out by the application of the observational operator. The relative differences for these layers all lie around ~0-  
486 20%. For the lowest two VMR bins we find again that CrIS gives larger results than the FTIR, around the CrIS  
487 sensitivity peak in the layer centred around 849 hPa, and to a lesser extent in the layer below. At these VMR  
488 levels ( $< 2$  ppb) the  $\text{NH}_3$  signal approaches the spectral noise of the CrIS measurement, making the retrievals  
489 more uncertain. The switch lies around 2-3 ppb where the difference in the SNR between the instruments  
490 becomes less of an issue. Also easily observed is the relation between the concentration and the absolute and  
491 relative differences. This can be explained by the difference in sensitivity of the instruments, and the  
492 measurement noise of both instruments. For the largest VMR bin [ $> 4.0$  ppb] we find that CrIS is biased for the  
493 four lowest layers. Differences are largest in the surface layer where only a few observations are available,  
494 almost all from the Bremen site. Most of these CrIS observations have a peak satellite sensitivity at a higher  
495 altitude than the FTIR. Assuming that most of the  $\text{NH}_3$  can be found directly near the surface, with the  
496 concentration dropping off with a sharp gradient as a function of altitude, it is likely that these concentrations  
497 are not directly observed by the satellite but are observed by the FTIR instruments. This difference in sensitivity  
498 should be at least partially removed by the application of the observational operator but not completely, due to  
499 the intrinsic differences between both retrievals. The CrIS retrieval uses one of three available a-priori profiles,  
500 which is chosen following a selection based on the strength of  $\text{NH}_3$  signature in the spectra. The three a-priori  
501 profiles (unpolluted, moderately polluted and polluted) are different in both shape and concentrations. Out of the  
502 entire set of 2047 combinations used in Fig. 8, only six are of the not polluted a priori category. About 1/3 of the  
503 remaining observations use the polluted a-priori, which has a sharper peak near the surface (see Fig. 5c),  
504 compared to the moderately polluted profile, which is used by 2/3s of the CrIS retrievals shown in this work.  
505 Based on the results as a function of retrieved VMR (as measured with the FTIR so not a perfect restriction), it  
506 is possible that the sharper peak at the surface as well as the low a-priori concentrations are restricting the  
507 retrieval. The dependence of the differences on VMR can also possibly follow from uncertainties in the line  
508 spectroscopy. In the lower troposphere there is a large gradient in pressure and temperature and the impact of  
509 any uncertainty in the line spectroscopy is greatly enhanced. Even for a day with large thermal contrast and  $\text{NH}_3$   
510 concentrations (e.g. Fig 5.), the difference between both the CrIS and FTIR retrievals was dominated by the line  
511 spectroscopy. This effect is further enhanced by the higher spectral resolution and reduced instrument noise of  
512 the FTIR instrument, which potentially makes it more able to resolve the line shapes.

513

514



515  
 516 **Figure 8.** Summary of differences as a function of maximum volume mixing ratio (VMR). The maximum VMR of each FTIR profiles is used for the  
 517 classification. Absolute (Top row) and relative profile differences (bottom row) following the FTIR and CrIS (FTIR - AVK applied) profiles. Observations are  
 518 following pressure layers, i.e. the midpoints of the CrIS pressure grid. The box edges are the 25<sup>th</sup> and 75<sup>th</sup> percentiles, the black line in the box is the median,  
 519 the red diamond is the mean, the whiskers are the 10<sup>th</sup> and 90<sup>th</sup> percentiles, and the grey circles are the outlier values outside the whiskers.



520 To summarise, the overall differences between both retrievals are quite small, except for the lowest layers in the  
521 NH<sub>3</sub> profile where CrIS has less sensitivity. The differences mostly follow the errors as estimated by the FTIR  
522 retrieval and further effort should focus on the estimated errors and uncertainties. A way to improve the  
523 validation would be to add a third set of measurements with a better capability to vertically resolve NH<sub>3</sub>  
524 concentrations from the surface up to ~750 hPa (i.e. the first 2500 m). One way to do this properly is probably  
525 by using airplane observations that could measure a spiral around the FTIR path coinciding with a CrIS  
526 overpass. The addition of the third set of observations would improve our capabilities to validate the satellite  
527 and FTIR retrievals and point out which retrieval specifically is causing the absolute and relative differences at  
528 each of the altitudes.

529

#### 530 4. Conclusions

531

532 Here we presented the first validation of the CrIS-NH<sub>3</sub> product using ground-based FTIR-NH<sub>3</sub> observations. The  
533 total column comparison shows that both retrievals agree well with a correlation of  $R = 0.77$  ( $P < 0.01$ ,  $N = 218$ )  
534 and almost no bias with an overall slope of  $1.02 (\pm 0.05)$ . For the individual stations we find varying levels of  
535 agreement mostly limited by the small range of NH<sub>3</sub> total columns. For FTIR total columns  $> 10 \times 10^{15}$   
536 molecules cm<sup>-2</sup> the CrIS and FTIR observations agree very well with only a small bias of  $0.4 (\pm 5.3) \times 10^{15}$   
537 molecules cm<sup>-2</sup>, and a relative difference  $4.57 (\pm 35.8) \%$ . In the smaller total column range the CrIS retrieval  
538 shows a positive bias with larger relative differences  $49.0 (\pm 62.6) \%$  that mostly seems to follow from  
539 observations near the CrIS detection limit. The results of the comparison between the FTIR and the IASI-NN  
540 and IASI-LUT retrievals, are comparable to those found in earlier studies. Both IASI products showed smaller  
541 total column values compared to the FTIR, with a MRD ~-35- -40%. On average, the CrIS retrieval has one  
542 piece of information, while the FTIR retrieval shows a bit more vertical information with DOFS in the range of  
543 1-2. The NH<sub>3</sub> profile comparison shows similar results, with a small mean negative difference between the CrIS  
544 and FTIR profiles for the surface layer and a positive difference for the layers above the surface layer. The  
545 relative and absolute differences in the retrieved profiles can be explained by the errors of the individual  
546 retrievals. Two causes of uncertainty stand out with the NH<sub>3</sub> line spectroscopy being the biggest factor, showing  
547 errors of up to 40% in the profile example. The second factor is the signal-to-noise ratio of both instruments  
548 which depends on the VMR: under large NH<sub>3</sub> concentrations, the FTIR uncertainty in the signal is in the range  
549 of 10%; for measurements with small NH<sub>3</sub> concentrations this greatly increases. Future work should focus on  
550 improvements to the NH<sub>3</sub> line spectroscopy to reduce the uncertainty coming from this error source.

551 Furthermore an increased effort is needed to acquire coincident measurements with the FTIR instruments during  
552 satellite overpasses as a dedicated validation effort will greatly enhance the number of available observations.  
553 Furthermore, a third type of observations measuring the vertical distribution of NH<sub>3</sub> could be used to compare  
554 with both the FTIR and CrIS retrievals and further constrain the differences. These observations could be  
555 provided by an airborne instrument flying spirals around an FTIR site during a satellite overpass.

556



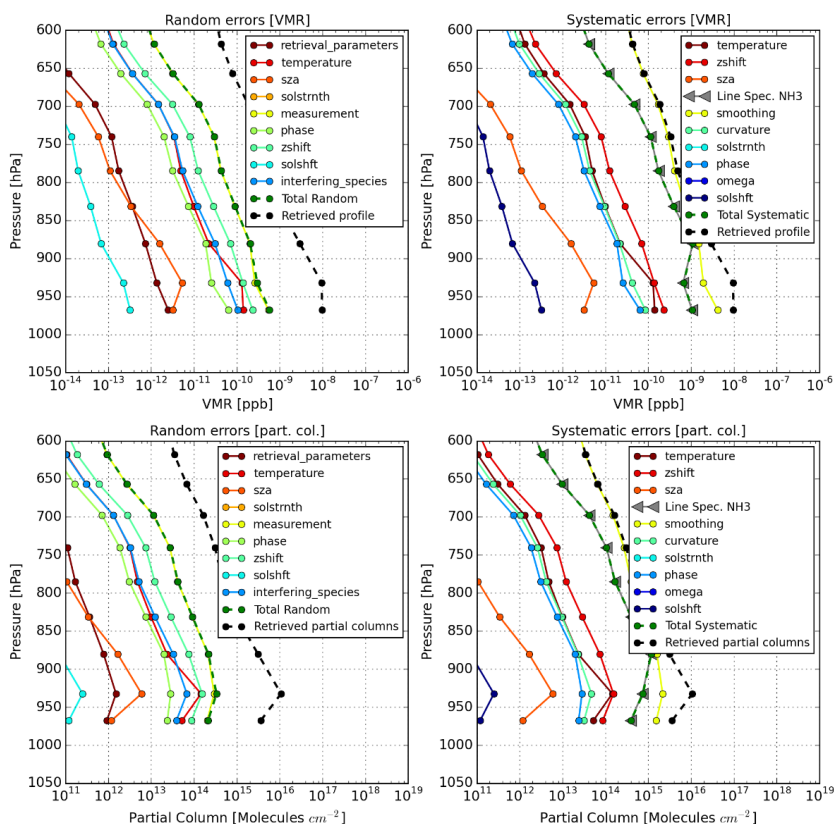
557 **5. Data availability**

558 FTIR-NH<sub>3</sub> data (Dammers et al., 2015) can be made available on request (M. Palm, Institut für Umweltphysik,  
 559 University of Bremen, Bremen, Germany). The CrIS-FRP-NH<sub>3</sub> science grade (non-operational) data products  
 560 used in this study can be made available on request (M. W. Shephard, Environment and Climate Change  
 561 Canada, Toronto, Ontario, Canada). The IASI-NH<sub>3</sub> product is freely available at [http://www.pole-](http://www.pole-ether.fr/etherTypo/index.php?id=1700&L=1)  
 562 [ether.fr/etherTypo/index.php?id=1700&L=1](http://www.pole-ether.fr/etherTypo/index.php?id=1700&L=1) (Van Damme et al., 2015a).

563

564 **6. Appendix A.**

FTIR Error summary: 20130709: Pasadena

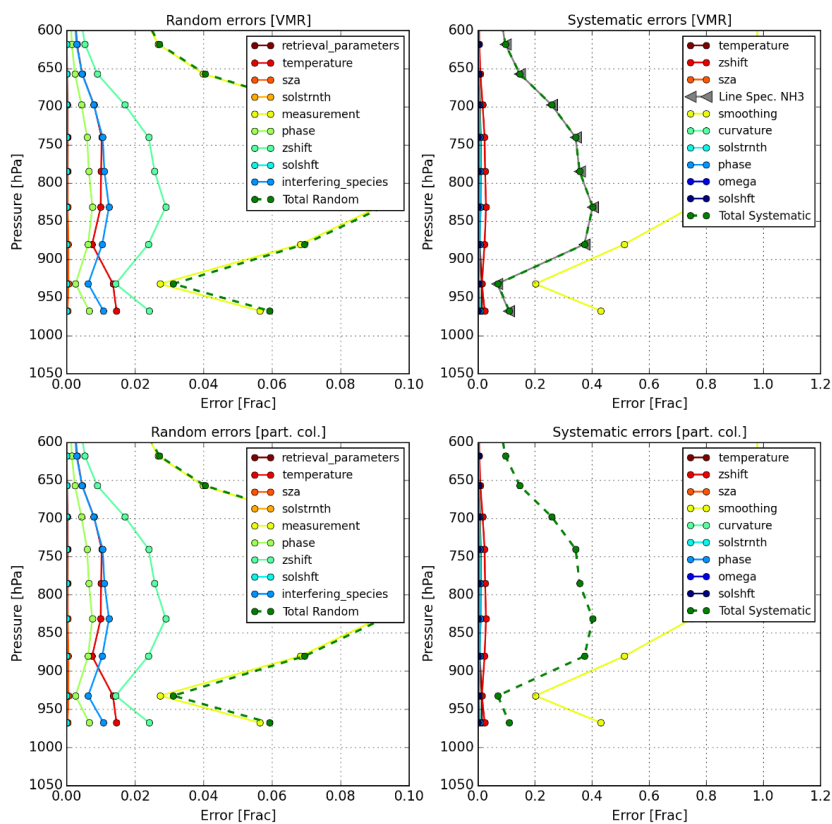


565

566 **Figure A1.** Error profiles for each of the error terms. Top panels show the random errors, bottom panels the  
 567 systematic errors. Left two panels show the error in VMR. Right panels show the errors in partial column layers  
 568 [molecules cm<sup>-2</sup>]. (See Figure A.2 for the same figure but with the errors relative to the final VMR and partial  
 569 columns per layer)



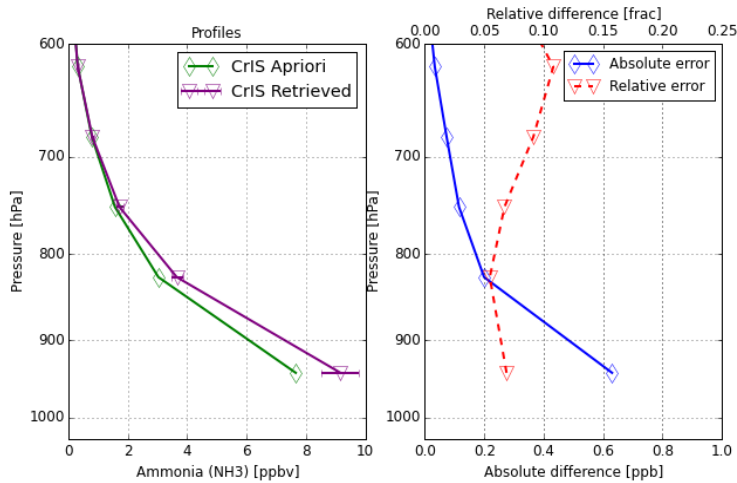
FTIR Error summary: 20130709: Pasadena



570

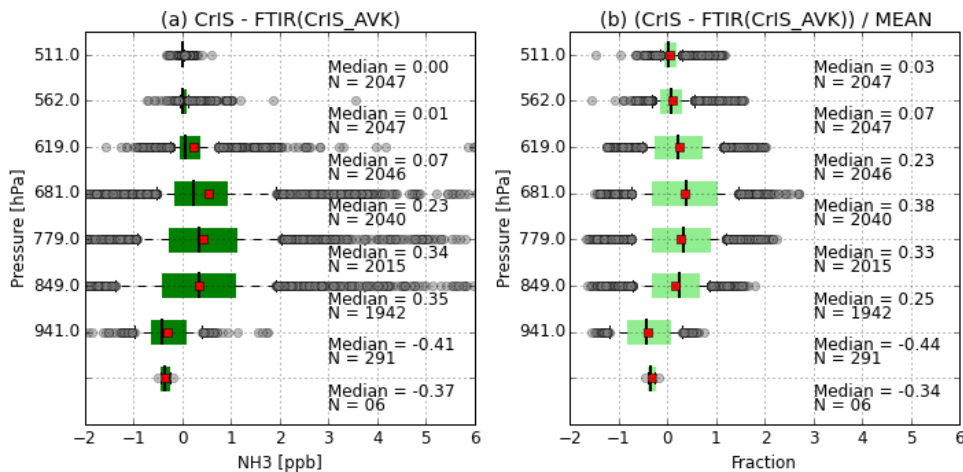
571 **Figure A2.** Relative error profiles for each of the error terms. Top panels show the Random errors, bottom  
 572 panels the Systematic errors. Left two panels show the error in VMR. Right panels show the errors in partial  
 573 column layers [molecules cm<sup>-2</sup>]. (See Figure A.1 for the same figure but with the absolute errors)

574



575  
 576  
 577  
 578  
 579

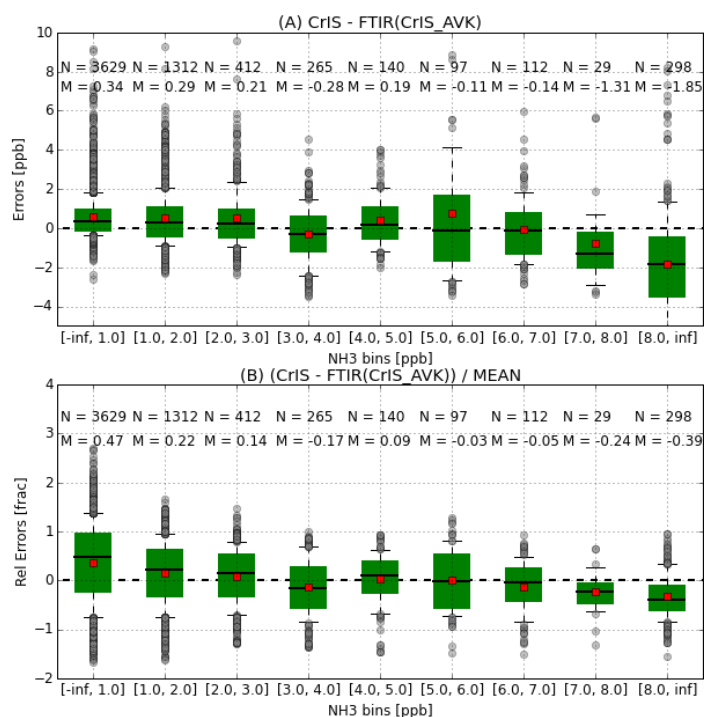
**Figure A3.** CrIS-NH<sub>3</sub> relative and absolute error profile. The left plot shows the retrieved and a-priori profiles similar to the profiles shown in Figure 5c. The right panel shows the measurement error on the CrIS retrieved profile, with the blue line the absolute value and red line the value relative to the retrieved profile.



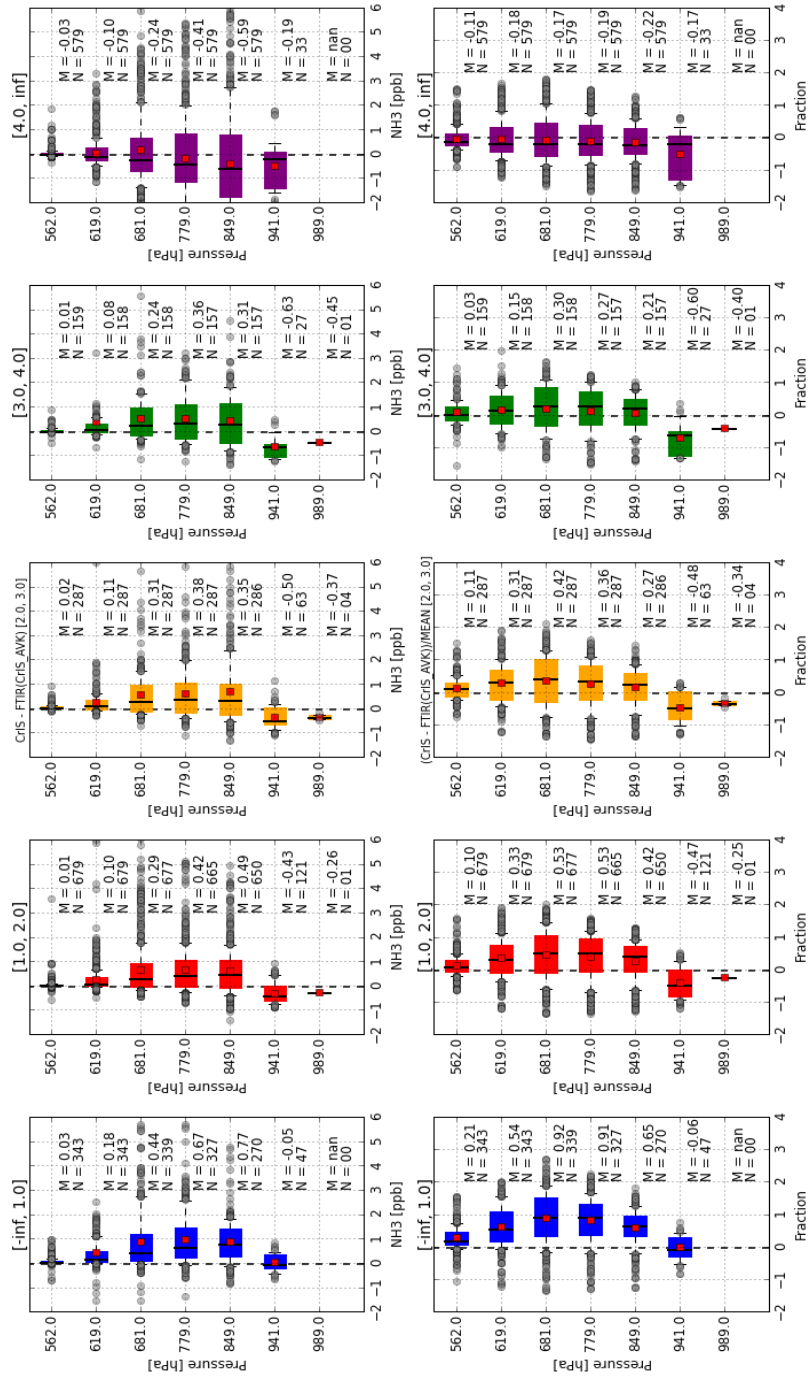
580  
 581  
 582  
 583  
 584  
 585  
 586  
 587

**Fig A4.** Profile comparison for all stations combined. Observations are combined following pressure “bins”, i.e. the midpoints of the CrIS pressure grid. Panel (a) shows the absolute difference [VMR] between profiles (f) and (a). Panel (b) shows the relative difference [Fraction] between the profiles in (Fig 6e) and (Fig 6b). Each of the boxes edges are the 25th and 75th percentiles, the black lines in each box is the median, the red diamond is the mean, the whiskers are the 10th and 90th percentiles, and the grey circles are the outlier values outside the whiskers.





588  
 589 **Fig A5.** Summary of the errors as a function of the VMR of NH<sub>3</sub> in the individual FTIR layers. The box edges  
 590 are the 25<sup>th</sup> and 75<sup>th</sup> percentiles, the black line in the box is the median, the red diamond is the mean, the  
 591 whiskers are the 10<sup>th</sup> and 90<sup>th</sup> percentiles, and the grey circles are the outlier values outside the whiskers. Only  
 592 observations with a pressure greater than 650 hPa are used. The top panel shows the absolute difference for each  
 593 VMR bin, the bottom panel shows the relative difference for each VMR bin.  
 594  
 595  
 596



597  
 598 **Fig A6.** Summary of errors as a function of VMR. The maximum VMR of each FTIR profiles is used for the classification. Absolute (Top row) and relative  
 599 profile differences (bottom row) following the FTIR (CrIS AVK applied) and CrIS profiles. Observations are following pressure layers, i.e. the midpoints of the  
 600 CrIS pressure grid. The box edges are the 25<sup>th</sup> and 75<sup>th</sup> percentiles, the black line in the box is the median, the red diamond is the mean, the whiskers are the  
 601 10<sup>th</sup> and 90<sup>th</sup> percentiles, and the grey circles are the outlier values outside the whiskers.



602 **Acknowledgements**

603

604 This work is part of the research programme GO/12-36, which is financed by the Netherlands Organisation for  
605 Scientific Research (NWO). This work was also funded at AER through a NASA funded  
606 (contract: NNH15CM65C). We would like to acknowledge the University of Wisconsin-Madison Space  
607 Science and Engineering Center Atmosphere SIPS team sponsored under NASA contract NNG15HZ38C for  
608 providing us with the CrIS level 1 and 2 input data, in particular Liam Gumley. We would also like to thank  
609 Andre Wehe (AER) and Jacob Siemons (ECCC) for developing the CrIS download and extraction software. The  
610 IASI-LUT and IASI-NN were obtained from the atmospheric spectroscopy group at ULB (Spectroscopie de  
611 l'Atmosphère, Service de Chimie Quantique et Photophysique, Université Libre de Bruxelles, Brussels,  
612 Belgium) and we would like to thank Simon Whitburn, Martin Van Damme, Lieven Clarisse and Pierre  
613 Francois Coheur for their help and contributions. Part of this work was performed at the Jet Propulsion  
614 Laboratory, California Institute of Technology, under contract with NASA. The University of Toronto FTIR  
615 retrievals were supported by the CAFTON project, funded by the Canadian Space Agency's FAST programme.  
616 Measurements were made at the University of Toronto Atmospheric Observatory (TAO), which has been  
617 supported by CFCAS, ABB Bomem, CFI, CSA, EC, NSERC, ORDCF, PREA, and the University of Toronto.  
618 Funding support in Mexico City was provided by UNAM-DGAPA grants IN107417 & IN112216. A. Bezanilla  
619 and B. Herrera participated in the FTIR measurements and M.A. Robles, W. Gutiérrez and M. García are  
620 thanked for technical support. We would also like to thank Roy Wichink Kruit and Margreet van Marle for the  
621 numerous discussions and valuable input on the subject.

622

623 **References**

624

- 625 Adams, P.J., Seinfeld, J.H., Koch, D., Mickley, L., Jacob, D. (2001), General circulation model assessment of  
626 direct radiative forcing by the sulfate-nitrate-ammonium-water inorganic aerosol system, *Journal of Geophysical*  
627 *Research Atmospheres*, 106 (1), pp. 1097-1111.  
628  
629 Alvarado, M. J., Payne, V. H., Mlawer, E. J., Uymin, G., Shephard, M. W., Cady-Pereira, K. E., Delamere, J. S.,  
630 and Moncet, J.-L.: Performance of the Line-By-Line Radiative Transfer Model (LBLRTM) for temperature,  
631 water vapor, and trace gas retrievals: recent updates evaluated with IASI case studies, *Atmos. Chem. Phys.*, 13,  
632 6687–6711, doi:10.5194/acp-13-6687-2013, 2013  
633  
634 Beer, R., Shephard, M. W., Kulawik, S. S., Clough, S. a., Eldering, A., Bowman, K. W., Sander, S. P., Fisher,  
635 B. M., Payne, V. H., Luo, M., Osterman, G. B. and Worden, J. R.: First satellite observations of lower  
636 tropospheric ammonia and methanol, *Geophys. Res. Lett.*, 35(9), 1–5, doi:10.1029/2008GL033642, 2008.  
637  
638 Bevington, P. R. and Robinson D. K. (1992) "Data Reduction and Error Analysis for the Physical Sciences, 2nd  
639 Ed." pp: 104, and 108-109, McGraw-Hill, New York.  
640  
641 Bezanilla A., Krueger A., Stremme W. and Grutter M. Solar absorption infrared spectroscopic measurements  
642 over Mexico City: Methane enhancements. *Atmósfera* 27(2), 173-183 (2014).  
643  
644 Bobbink, R, Hicks K, Galloway J, Spranger T, Alkemade R, Ashmore M, Bustamante M, Cinderby S, Davidson  
645 E, Dentener F, Emmett B, Erisman JW, Fenn M, Gilliam F, Nordin A, Pardo L, De Vries W. Global assessment  
646 of nitrogen deposition effects on terrestrial plant diversity: a synthesis, *Ecological Applications*, 20 (2010), pp.  
647 30–59.  
648  
649 von Bobrutzki, K., Braban, C. F., Famulari, D., Jones, S. K., Blackall, T., Smith, T. E. L., Blom, M., Coe, H.,  
650 Gallagher, M., Ghalaieny, M., McGillen, M. R., Percival, C. J., Whitehead, J. D., Ellis, R., Murphy, J., Mohacsi,



- 651 A., Pogany, A., Junninen, H., Rantanen, S., Sutton, M. A., and Nemitz, E.: Field inter-comparison of eleven  
 652 atmospheric ammonia measurement techniques, *Atmos. Meas. Tech.*, 3, 91-112, doi:10.5194/amt-3-91-2010,  
 653 2010.
- 654
- 655 Brown, L. R., M. R. Gunson, R. A. Toth, F. W. Irion, C. P. Rinsland, and A. Goldman. "1995 atmospheric trace  
 656 molecule spectroscopy (ATMOS) linelist." *Applied optics* 35, no. 16 (1996): 2828-2848.
- 657
- 658 Calisesi, Y., V. T. Soebijanta, and R. van Oss (2005), Regridding of remote soundings: Formulation and  
 659 application to ozone profile comparison, *J. Geophys. Res.*, 110, D23306, doi:10.1029/2005JD006122.
- 660
- 661 Chang, L., Palo, S., Hagan, M., Richter, J., Garcia, R., Riggin, D. and Fritts, D.: Structure of the migrating  
 662 diurnal tide in the Whole Atmosphere Community Climate Model (WACCM), *Advances in Space Research*,  
 663 41(9), 1398–1407, doi:10.1016/j.asr.2007.03.035, 2008.
- 664
- 665 Clarisse, Lieven, Cathy Clerbaux, Frank Dentener, Daniel Hurtmans, and Pierre-François Coheur. "Global  
 666 ammonia distribution derived from infrared satellite observations." *Nature Geoscience* 2, no. 7 (2009): 479-483.
- 667
- 668 Clarisse, L., Shephard, M. W., Dentener, F., Hurtmans, D., Cady-Pereira, K., Karagulian, F., Van Damme, M.,  
 669 Clerbaux, C. and Coheur, P.-F.: Satellite monitoring of ammonia: A case study of the San Joaquin Valley, *J.*  
 670 *Geophys. Res.*, 115(D13), 1–15, doi:10.1029/2009JD013291, 2010.
- 671
- 672 Clough, S. A., Shephard, M. W., Mlawer, E. J., Delamere, J. S., Iacono, M. J., Cady-Pereira, K., Boukabara, S.,  
 673 and Brown, P. D.: Atmospheric radiative transfer modeling: a summary of the AER codes, *J. Quant. Spectrosc.*  
 674 *Radiat. T.*, 91, 233–244, 2005.
- 675
- 676 Coheur, P.-F., Clarisse, L., Turquety, S., Hurtmans, D., and Clerbaux, C.: IASI measurements of reactive trace  
 677 species in biomass burning plumes, *Atmos. Chem. Phys.*, 9, 5655-5667, doi:10.5194/acp-9-5655-2009, 2009.
- 678
- 679 Dammers, E., Vigouroux, C., Palm, M., Mahieu, E., Warneke, T., Smale, D., Langerock, B., Franco, B., Van  
 680 Damme, M., Schaap, M., Notholt, J., and Erisman, J. W.: Retrieval of ammonia from ground-based FTIR solar  
 681 spectra, *Atmos. Chem. Phys.*, 15, 12789-12803, doi:10.5194/acp-15-12789-2015, 2015.
- 682
- 683 Dammers, E., Palm, M., Van Damme, M., Vigouroux, C., Smale, D., Conway, S., Toon, G. C., Jones, N.,  
 684 Nussbaumer, E., Warneke, T., Petri, C., Clarisse, L., Clerbaux, C., Hermans, C., Lutsch, E., Strong, K.,  
 685 Hannigan, J. W., Nakajima, H., Morino, I., Herrera, B., Stremme, W., Grutter, M., Schaap, M., Wichink Kruit,  
 686 R. J., Notholt, J., Coheur, P.-F., and Erisman, J. W.: An evaluation of IASI-NH<sub>3</sub> with ground-based Fourier  
 687 transform infrared spectroscopy measurements, *Atmos. Chem. Phys.*, 16, 10351-10368, doi:10.5194/acp-16-  
 688 10351-2016, 2016a.
- 689
- 690 Dammers, E., Palm, M., Van Damme, M., Shephard, M., Cady-Pereira, K., Capps, S., Clarisse, L., Coheur, P.  
 691 and Erisman, J. W.: Validation of NH<sub>3</sub> satellite observations by ground-based FTIR measurements, in EGU  
 692 General Assembly Conference Abstracts, vol. 18, p. 1657., 2016b.
- 693
- 694 Dentener, F., Drevet, J., Lamarque, J. F., Bey, I., Eickhout, B., Fiore, A. M., Hauglustaine, D., Horowitz, L. W.,  
 695 Krol, M., Kulshrestha, U. C., Lawrence, M., Galy-Lacaux, C., Rast, S., Shindell, D., Stevenson, D., Van Noije,  
 696 T., Atherton, C., Bell, N., Bergman, D., Butler, T., Cofala, J., Collins, B., Doherty, R., Ellingsen, K., Galloway,  
 697 J., Gauss, M., Montanaro, V., Müller, J. F., Pitari, G., Rodriguez, J., Sanderson, M., Solomon, F., Strahan, S.,  
 698 Schultz, M., Sudo, K., Szopa, S. and Wild, O.: Nitrogen and sulfur deposition on regional and global scales: A  
 699 multimodel evaluation, *Global Biogeochem. Cycles*, 20(4), doi:10.1029/2005GB002672, 2006.
- 700
- 701 Erisman, J. W., Bleeker, a., Galloway, J. and Sutton, M. S.: Reduced nitrogen in ecology and the environment,  
 702 *Environ. Pollut.*, 150(1), 140–149, doi:10.1016/j.envpol.2007.06.033, 2007.
- 703
- 704 Erisman, J.W., Sutton, M.A., Galloway, J., Klimont, Z. and Winiwarter, W., 2008. How a century of ammonia  
 705 synthesis changed the world. *Nature Geoscience*, 1(10), pp.636-639.
- 706
- 707 Erisman, J. W., Galloway, J., Seitzinger, S., Bleeker, A. and Butterbach-Bahl, K.: Reactive nitrogen in the  
 708 environment and its effect on climate change, *Curr. Opin. Environ. Sustain.*, 3(5), 281–290,  
 709 doi:10.1016/j.cosust.2011.08.012, 2011.
- 710



- 711 Farr, T. G., Rosen, P. a., Caro, E. and Crippen, R.: The Shuttle Radar Topography Mission, Rev. ...., (2005), 1–  
 712 33, doi:10.1029/2005RG000183.1.INTRODUCTION, 2007.
- 713
- 714 Fowler, D., Coyle, M., Skiba, U., Sutton, M. A., Cape, J. N., Reis, S., Sheppard, L. J., Jenkins, A., Grizzetti, B.,  
 715 Galloway, J. N., Vitousek, P., Leach, A., Bouwman, A. F., Butterbach-Bahl, K., Dentener, F., Stevenson, D.,  
 716 Amann, M. and Voss, M.: The global nitrogen cycle in the twenty-first century, Philos. Trans. R. Soc. London B  
 717 Biol. Sci., 368(1621) [online] Available from:  
 718 <http://rstb.royalsocietypublishing.org/content/368/1621/20130164.abstract>, 2013.
- 719
- 720 Hase, F., Hannigan, J. W., Coffey, M. T., Goldman, a., Höpfner, M., Jones, N. B., Rinsland, C. P. and Wood, S.  
 721 W.: Intercomparison of retrieval codes used for the analysis of high-resolution, ground-based FTIR  
 722 measurements, J. Quant. Spectrosc. Radiat. Transf., 87(1), 25–52, doi:10.1016/j.jqsrt.2003.12.008, 2004.
- 723
- 724 Hase, F., Demoulin, P., Sauval, A. J., Toon, G. C., Bernath, P. F., Goldman, A., Hannigan, J. W., Rinsland, C.  
 725 P.: An empirical line-by-line model for the infrared solar transmittance spectrum from 700 to 5000 cm<sup>-1</sup>, J.  
 726 Quant. Spectrosc. Ra., 102, 450–463, doi:10.1016/j.jqsrt.2006.02.026, 2006.
- 727
- 728 Heald, C. L., Collett Jr., J. L., Lee, T., Benedict, K. B., Schwandner, F. M., Li, Y., Clarisse, L., Hurtmans, D. R.,  
 729 Van Damme, M., Clerbaux, C., Coheur, P.-F., Philip, S., Martin, R. V., and Pye, H. O. T.: Atmospheric  
 730 ammonia and particulate inorganic nitrogen over the United States, Atmos. Chem. Phys., 12, 10295-10312,  
 731 doi:10.5194/acp-12-10295-2012, 2012
- 732
- 733 Holland, E. a., Dentener, F. J., Braswell, B. H. and Sulzman, J. M.: Contemporary and pre-industrial global  
 734 reactive nitrogen budgets, Biogeochemistry, 46(1-3), 7–43, doi:10.1007/BF01007572, 1999.
- 735
- 736 Leen, J. B., Yu, X. Y., Gupta, M., Baer, D. S., Hubbe, J. M., Kluzek, C. D., Tomlinson, J. M. and Hubbell, M.  
 737 R.: Fast in situ airborne measurement of ammonia using a mid-infrared off-axis ICOS spectrometer, Environ.  
 738 Sci. Technol., 47(18), 10446–10453, doi:10.1021/es401134u, 2013.
- 739
- 740 Lonsdale, C. R., Hegarty, J. D., Cady-Pereira, K., Alvarado, M. J., Henze, D. K., Turner, M. D., Capps, S. L.,  
 741 Nowak, J. B., Neuman, J. A., Middlebrook, A. M., Bahreini, R., Murphy, J. G., Markovic, M., VandenBoer, T.  
 742 C., Russell, L. M., and Scarino, A. J.: Modeling the Diurnal Variability of Agricultural Ammonia in Bakersfield,  
 743 California during CalNex, Atmos. Chem. Phys. Discuss., doi:10.5194/acp-2016-44, in review, 2016
- 744
- 745 Lutsch, E., Dammers, E., Conway, S. and Strong, K., 2016. Long-range transport of NH<sub>3</sub>, CO, HCN, and C<sub>2</sub>H<sub>6</sub>  
 746 from the 2014 Canadian Wildfires. Geophysical Research Letters, 43(15), pp.8286-8297,  
 747 doi:10.1002/2016GL070114, 2016.
- 748
- 749 Miller, D. J., Sun, K., Tao, L., Khan, M. A., and Zondlo, M. A.: Open-path, quantum cascade-laser-based sensor  
 750 for high-resolution atmospheric ammonia measurements, Atmos. Meas. Tech., 7, 81-93, doi:10.5194/amt-7-81-  
 751 2014, 2014
- 752
- 753 Moncet, J.-L., X. Liu, H. Snell, J. Eluszkiewicz, Y. He, T. Knelly, R. Lynch, S. Boukabara, A. Lipton, H.  
 754 Rieu-Isaacs, G. Uymin, and S. Zaccheo : Algorithm Theoretical Basis Document for the Cross-track Infrared  
 755 Sounder Environmental Data Records, AER Document Number: P1187-TR-I-08, Version 4.2, available at:  
 756 [http://www.star.nesdis.noaa.gov/jpss/documents/ATBD/D0001-M01-S01-007\\_JPSS\\_ATBD\\_CrIMSS\\_B.pdf](http://www.star.nesdis.noaa.gov/jpss/documents/ATBD/D0001-M01-S01-007_JPSS_ATBD_CrIMSS_B.pdf),  
 757 (last access date: 24 October 2015), 2005.
- 758
- 759 Moncet, J.-L., Uymin G., Lipton A. E., and Snell H. E.: Infrared radiance modeling by optimal spectral  
 760 sampling. J. Atmos. Sci., 65, 3917-3934, 2008.
- 761
- 762 Morgenstern, O., Zeng, G., Wood, S. W., Robinson, J., Smale, D., Paton-Walsh, C., Jones, N. B., and Griffith,  
 763 D. W. T.: Long-range correlations in Fourier transform infrared, satellite, and modeled CO in the Southern  
 764 Hemisphere, J. Geophys. Res., 117, D11301 doi:10.1029/2012JD017639, 2012.
- 765
- 766 Myhre, G., Shindell, D., Bréon, F.-M., Collins, W., Fuglested, J., Huang, J., Koch, D., Lamarque, J.-F., Lee,  
 767 D., Mendoza, B., Nakajima, T., Robock, A., Stephens, G., Takemura, T., and Zhang, H.: Anthropogenic and  
 768 Natural Radiative Forcing, in: Climate Change 2013: The Physical Science Basis. Contribution of Working  
 769 Group I to the Fifth Assessment Report of the Intergovernmental Panel on Climate Change, edited by: Stocker,



- 770 T. F., Qin, D., Plattner, G.-K., Tignor, M., Allen, S. K., Boschung, J., Nauels, A., Xia, Y., Bex, V., and Midgley,  
 771 P. M., Cambridge University Press, Cambridge, United Kingdom and New York, NY, USA, 2013  
 772
- 773 Nowak, J. B., Neuman, J. A., Kozai, K., Huey, L. G., Tanner, D. J., Holloway, J. S., Ryerson, T. B., Frost, G. J.,  
 774 McKeen, S. A., and Fehsenfeld, F. C.: A chemical ionization mass spectrometry technique for airborne  
 775 measurements of ammonia, *J. Geophys. Res.-Atmos.*, 112, D10S02, doi:10.1029/2006JD007589, 2007.  
 776
- 777 Nowak, J. B., Neuman, J. A., Bahreini, R., Brock, C. A., Middlebrook, A. M., Wollny, A. G., Holloway, J. S.,  
 778 Peischl, J., Ryerson, T. B., and Fehsenfeld, F. C.: Airborne observations of ammonia and ammonium nitrate  
 779 formation over Houston, Texas, *J. Geophys. Res.-Atmos.*, 115, D22 304, doi:10.1029/2010JD014195, 2010.  
 780
- 781 Nowak, J. B., Neuman, J. A., Bahreini, R., Middlebrook, A. M., Holloway, J. S., McKeen, S. A., Parrish, D. D.,  
 782 Ryerson, T. B. and Trainer, M.: Ammonia sources in the California South Coast Air Basin and their impact on  
 783 ammonium nitrate formation, *Geophys. Res. Lett.*, 39(7), 2012.  
 784
- 785 Oren, R., Ellsworth, D.S., Johnsen, K.H., Phillips, N., Ewers, B.E., Maier, C., Schäfer, K.V., McCarthy, H.,  
 786 Hendrey, G., McNulty, S.G. and Katul, G.G., 2001. Soil fertility limits carbon sequestration by forest  
 787 ecosystems in a CO<sub>2</sub>-enriched atmosphere. *Nature*, 411(6836), pp.469-472.  
 788
- 789 Pope III, C. A., Burnett, R. T., Thun, M. J., Calle, E. E., Krewski, D., Ito, K. and Thurston, G. D.: Lung cancer,  
 790 cardiopulmonary mortality, and long-term exposure to fine particulate air pollution, *Jama*, 287(9), 1132–1141,  
 791 2002.  
 792
- 793 Pope, III, C. A., Ezzati, M., and Dockery, D. W.: Fine-Particulate Air Pollution and Life Expectancy in the  
 794 United States, *N. Engl. J. Med.*, 360, 376–386, doi:{10.1056/NEJMsa0805646}, 2009.  
 795
- 796 Pougatchev, N. S., Connor, B. J., & Rinsland, C. P. (1995). Infrared measurements of the ozone vertical  
 797 distribution above Kitt Peak. *Journal of Geophysical Research: Atmospheres* (1984–2012), 100(D8), 16689-  
 798 16697.  
 799
- 800 Puchalski, M. A., M. E. Sather, J. T. Walker, C. M. Lehmann, D. A. Gay, J. Mathew, and W. P. Robarge (2011),  
 801 Passive ammonia monitoring in the United States: Comparing three different sampling devices, *J. Environ.*  
 802 *Monit.*, 13(11), 3156–3167, doi:10.1039/c1em10553a.  
 803
- 804 Reis, S., Pinder, R. W., Zhang, M., Lijje, G., and Sutton, M. A.: Reactive nitrogen in atmospheric emission  
 805 inventories, *Atmos. Chem. Phys.*, 9, 7657-7677, doi:10.5194/acp-9-7657-2009, 2009  
 806
- 807 Rockstrom, J., Steffen, W., Noone, K., Persson, A., Chapin, F. S., Lambin, E. F., Lenton, T. M., Scheffer, M.,  
 808 Folke, C., Schellnhuber, H. J., Nykvist, B., de Wit, C. A., Hughes, T., van der Leeuw, S., Rodhe, H., Sorlin, S.,  
 809 Snyder, P. K., Costanza, R., Svedin, U., Falkenmark, M., Karlberg, L., Corell, R. W., Fabry, V. J., Hansen, J.,  
 810 Walker, B., Liverman, D., Richardson, K., Crutzen, P. and Foley, J. A.: A safe operating space for humanity,  
 811 *Nature*, 461(7263), 472–475 [online] Available from: <http://dx.doi.org/10.1038/461472a>, 2009.  
 812
- 813 Rodgers, C. D.: Inverse methods for atmospheric Sounding: Theory and Practice, World Sci., Hackensack, NJ,  
 814 2000.  
 815
- 816 Rodgers, C. D. and Connor, B. J.: Intercomparison of remote sounding instruments, *J. Geophys. Res. Atmos.*,  
 817 108(D3), n/a–n/a, doi:10.1029/2002JD002299, 2003.  
 818
- 819 Rodhe, Henning, Frank Dentener, and Michael Schulz. "The global distribution of acidifying wet deposition."  
 820 *Environmental Science & Technology* 36.20 (2002): 4382-4388.  
 821
- 822 Rothman, L. S., Gordon, I. E., Babikov, Y., Barbe, a., Chris Benner, D., Bernath, P. F., Birk, M., Bizzocchi, L.,  
 823 Boudon, V., Brown, L. R., Campargue, a., Chance, K., Cohen, E. a., Coudert, L. H., Devi, V. M., Drouin, B. J.,  
 824 Fayt, a., Flaud, J. M., Gamache, R. R., Harrison, J. J., Hartmann, J. M., Hill, C., Hodges, J. T., Jacquemart, D.,  
 825 Jolly, a., Lamouroux, J., Le Roy, R. J., Li, G., Long, D. a., Lyulin, O. M., Mackie, C. J., Massie, S. T.,  
 826 Mikhailenko, S., Müller, H. S. P., Naumenko, O. V., Nikitin, a. V., Orphal, J., Perevalov, V., Perrin, a.,  
 827 Polovtseva, E. R., Richard, C., Smith, M. a H., Starikova, E., Sung, K., Tashkun, S., Tennyson, J., Toon, G. C.,  
 828 Tyuterev, V. G. and Wagner, G.: The HITRAN2012 molecular spectroscopic database, *J. Quant. Spectrosc.*  
 829 *Radiat. Transf.*, 130, 4–50, doi:10.1016/j.jqsrt.2013.07.002, 2013.



- 830  
 831 Schaap, M., van Loon, M., ten Brink, H. M., Dentener, F. J., and Builtjes, P. J. H.: Secondary inorganic aerosol  
 832 simulations for Europe with special attention to nitrate, *Atmos. Chem. Phys.*, 4, 857–874, doi:10.5194/acp-4-  
 833 857-2004, 2004.  
 834  
 835 Schiferl, L. D., Heald, C. L., Nowak, J. B., Holloway, J. S., Neuman, J. A., Bahreini, R., Pollack, I. B., Ryerson,  
 836 T. B., Wiedinmyer, C., and Murphy, J. G.: An investigation of ammonia and inorganic particulate matter in  
 837 California during the CalNex campaign, *J. Geophys. Res.-Atmos.*, 119, 1883–1902,  
 838 doi:10.1002/2013JD020765, 2014.  
 839  
 840 Schiferl, L. D., Heald, C. L., Van Damme, M., Clarisse, L., Clerbaux, C., Coheur, P.-F., Nowak, J. B., Neuman,  
 841 J. A., Herndon, S. C., Roscioli, J. R., and Eilerman, S. J.: Interannual variability of ammonia concentrations  
 842 over the United States: sources and implications, *Atmos. Chem. Phys.*, 16, 12305–12328, doi:10.5194/acp-16-  
 843 12305-2016, 2016  
 844  
 845 Seinfeld, J. H. and Pandis, S. N.: *Atmospheric Chemistry and Physics*, John Wiley, Hoboken, NJ, 1988.  
 846  
 847 Shephard, M.W., Clough, S. A., Payne, V. H., Smith, W. L., Kireev, S., and Cady-Pereira, K. E.: Performance of  
 848 the line-by-line radiative transfer model (LBLRTM) for temperature and species retrievals: IASI case studies  
 849 from JAIVEx, *Atmos. Chem. Phys.*, 9, 7397–7417, doi:10.5194/acp-9-7397-2009, 2009.  
 850  
 851 Shephard, M. W., Cady-Pereira, K. E., Luo, M., Henze, D. K., Pinder, R. W., Walker, J. T., Rinsland, C. P.,  
 852 Bash, J. O., Zhu, L., Payne, V. H., and Clarisse, L.: TES ammonia retrieval strategy and global observations of  
 853 the spatial and seasonal variability of ammonia, *Atmos. Chem. Phys.*, 11, 10743–10763, doi:10.5194/acp-11-  
 854 10743-2011, 2011  
 855  
 856 Shephard, M. W. and Cady-Pereira, K. E.: Cross-track Infrared Sounder (CrIS) satellite observations of  
 857 tropospheric ammonia, *Atmos. Meas. Techn.*, 8, 1323–1336, doi:10.5194/amt-8-1323-2015, [http://www.  
 858 atmos-meas-tech.net/8/1323/2015/](http://www.atmos-meas-tech.net/8/1323/2015/), 2015.  
 859  
 860 Shephard, M. W., McLinden, C. A., Cady-Pereira, K. E., Luo, M., Moussa, S. G., Leithead, A., Liggio, J.,  
 861 Staebler, R. M., Akingunola, A., Makar, P., Lehr, P., Zhang, J., Henze, D. K., Millet, D. B., Bash, J. O., Zhu, L.,  
 862 Wells, K. C., Capps, S. L., Chaliyakunnel, S., Gordon, M., Hayden, K., Brook, J. R., Wolde, M., and Li, S.-M.:  
 863 Tropospheric Emission Spectrometer (TES) satellite observations of ammonia, methanol, formic acid, and  
 864 carbon monoxide over the Canadian oil sands: validation and model evaluation, *Atmos. Meas. Tech.*, 8, 5189-  
 865 5211, doi:10.5194/amt-8-5189-2015, 2015.  
 866  
 867 Sun, K., Cady-Pereira, K., Miller, D. J., Tao, L., Zondlo, M.A., Nowak, J. B., Neuman, J. A., Mikoviny, T.,  
 868 Müller, M., Wisthaler, A., Scarino, A. J., and Hostetler, C. A.: Validation of TES ammonia observations at the  
 869 single pixel scale in the San Joaquin Valley during DISCOVER-AQ, *J. Geophys. Res.-Atmos.*, 120, 5140–5154,  
 870 doi:10.1002/2014JD022846, 2015.  
 871  
 872  
 873 Sutton, M. a, Reis, S., Riddick, S. N., Dragosits, U., Nemitz, E., Theobald, M. R., Tang, Y. S., Braban, C. F.,  
 874 Vieno, M., Dore, A. J., Mitchell, R. F., Wanless, S., Daunt, F., Fowler, D., Blackall, T. D., Milford, C.,  
 875 Flechard, C. R., Loubet, B., Massad, R., Cellier, P., Personne, E., Coheur, P. F., Clarisse, L., Van Damme, M.,  
 876 Ngadi, Y., Clerbaux, C., Skjøth, C. A., Geels, C., Hertel, O., Wichink Kruit, R. J., Pinder, R. W., Bash, J. O.,  
 877 Walker, J. T., Simpson, D., Horváth, L., Misselbrook, T. H., Bleeker, A., Dentener, F. and de Vries, W.:  
 878 Towards a climate-dependent paradigm of ammonia emission and deposition., *Philos. Trans. R. Soc. Lond. B.*  
 879 *Biol. Sci.*, 368(1621), 20130166, doi:10.1098/rstb.2013.0166, 2013.  
 880  
 881 Tobin, D.: Early Checkout of the Cross-track Infrared Sounder (CrIS) on Suomi-NPP, Through the  
 882 Atmosphere, Summer 2012, available at: [www.ssec.wisc.edu/news/media/2012/07/ttasummer20121.pdf](http://www.ssec.wisc.edu/news/media/2012/07/ttasummer20121.pdf)  
 883 (last access date: 30 January 2017), 2012.  
 884  
 885 Toon, G. C., Blavier, J.-F., Sen, B., Margitan, J. J., Webster, C. R., Max, R. D., Fahey, D. W., Gao, R.,  
 886 DelNegro, L., Proffitt, M., Elkins, J., Romashkin, P. A., Hurst, D. F., Oltmans, S., Atlas, E., Schauffler, S.,  
 887 Flocke, F., Bui, T. P., Stimpfle, R. M., Bonne, G. P., Voss, P. B., and Cohen, R. C.: Comparison of MkIV  
 888 balloon and ER-2 aircraft measurements of atmospheric trace gases, *J. Geophys. Res.*, 104, 26 779–26 790,  
 889 1999.



- 890  
 891 Van Damme, M., Clarisse, L., Heald, C. L., Hurtmans, D., Ngadi, Y., Clerbaux, C., Dolman, A. J., Erisman, J.  
 892 W., and Coheur, P. F.: Global distributions, time series and error characterization of atmospheric ammonia  
 893 (NH<sub>3</sub>) from IASI satellite observations, *Atmos. Chem. Phys.*, 14, 2905–2922, doi:10.5194/acp-14-2905-2014,  
 894 2014a.
- 895  
 896 Van Damme, M., R. J. Wichink Kruit, M. Schaap, L. Clarisse, C. Clerbaux, P.-F. Coheur, E. Dammers, A. J.  
 897 Dolman, and J. W. Erisman, Evaluating 4 years of atmospheric ammonia (NH<sub>3</sub>) over Europe using IASI  
 898 satellite observations and LOTOS-EUROS model results, *J. Geophys. Res. Atmos.*, 119, 9549–9566,  
 899 doi:10.1002/2014JD021911, 2014b.
- 900  
 901 Van Damme, M., J. W. Erisman, L. Clarisse, E. Dammers, S. Whitburn, C. Clerbaux, A. J. Dolman, and P.-F.  
 902 Coheur (2015a), Worldwide spatiotemporal atmospheric ammonia (NH<sub>3</sub>) columns variability revealed by  
 903 satellite, *Geophys. Res. Lett.*, 42, doi:10.1002/2015GL065496.
- 904  
 905 Van Damme, M., Clarisse, L., Dammers, E., Liu, X., Nowak, J. B., Clerbaux, C., Flechard, C. R., Galy-Lacaux,  
 906 C., Xu, W., Neuman, J. a., Tang, Y. S., Sutton, M. a., Erisman, J. W. and Coheur, P. F.: Towards validation of  
 907 ammonia (NH<sub>3</sub>) measurements from the IASI satellite, *Atmos. Meas. Tech.*, 8(3), 1575–1591, doi:10.5194/amt-  
 908 8-1575-2015, 2015b.
- 909  
 910 Velazco, V., Wood, S. W., Sinnhuber, M., Kramer, I., Jones, N. B., Kasai, Y., Notholt, J., Warneke, T.,  
 911 Blumenstock, T., Hase, F., Murcray, F. J., and Schrems, O.: Annual variation of strato-mesospheric carbon  
 912 monoxide measured by ground-based Fourier transform infrared spectrometry, *Atmos. Chem. Phys.*, 7, 1305-  
 913 1312, doi:10.5194/acp-7-1305-2007, 2007.
- 914  
 915 Warner, J. X., Wei, Z., Strow, L. L., Dickerson, R. R., and Nowak, J. B.: The global tropospheric ammonia  
 916 distribution as seen in the 13-year AIRS measurement record, *Atmos. Chem. Phys.*, 16, 5467–5479,  
 917 doi:10.5194/acp-16-5467-2016, 2016
- 918  
 919 Whitburn, S., Van Damme, M., Kaiser, J. W., van der Werf, G. R., Turquety, S., Hurtmans, D., Clarisse, L.,  
 920 Clerbaux, C. and Coheur, P.-F.: Ammonia emissions in tropical biomass burning regions: Comparison between  
 921 satellite-derived emissions and bottom-up fire inventories, *Atmos. Environ.*, 1–13,  
 922 doi:10.1016/j.atmosenv.2015.03.015, 2015.
- 923  
 924 Whitburn, S., M. Van Damme, L. Clarisse, S. Bauduin, C. L. Heald, J. Hadji-Lazaro, D. Hurtmans, M. A.  
 925 Zondlo, C. Clerbaux, and P.-F. Coheur (2016), A flexible and robust neural network IASI-NH<sub>3</sub> retrieval  
 926 algorithm, *J. Geophys. Res. Atmos.*, 121, 6581–6599, doi:10.1002/2016JD024828.
- 927  
 928 Wiacek, A., Taylor, J. R., Strong, K., Saari, R., Kerzenmacher, T. E., Jones, N. B. and Griffith, D. W. T.:  
 929 Ground-Based Solar Absorption FTIR Spectroscopy: Characterization of Retrievals and First Results from a  
 930 Novel Optical Design Instrument at a New NDACC Complementary Station, *J. Atmos. Ocean. Technol.*, 24(3),  
 931 432–448, doi:10.1175/JTECH1962.1, 2007.
- 932  
 933 Worden, J., Kulawik S. S., Shephard M. W., Clough S. A., Worden H., Bowman K., and Goldman A.: Predicted  
 934 errors of tropospheric emission spectrometer nadir retrievals from spectral window selection, *J. Geophys. Res.*,  
 935 109, D09308, doi:10.1029/2004JD004522, 2004.
- 936  
 937  
 938 Zondlo, M., Pan, D., Golston, L., Sun, K. and Tao, L.: Ammonia emissions, transport, and deposition downwind  
 939 of agricultural areas at local to regional scales, in EGU General Assembly Conference Abstracts, vol. 18, p.  
 940 16552., 2016.
- 941  
 942 Zhu, L., Henze, D. K., Cady-Pereira, K. E., Shephard, M. W., Luo, M., Pinder, R. W., Bash, J. O. and Jeong, G.  
 943 R.: Constraining U.S. ammonia emissions using TES remote sensing observations and the GEOS-Chem adjoint  
 944 model, *J. Geophys. Res. Atmos.*, 118(8), 3355–3368, doi:10.1002/jgrd.50166, 2013.
- 945